

UNIVERSITY OF COLORADO AT BOULDER

UNDERGRADUATE THESIS

**Statistical Modeling and Beam Analysis
for the Redshifted Global 21 Centimeter
Signal**

By

Katherine June Pellicore

Department of Astrophysical and Planetary Sciences

*A thesis submitted to the faculty of the University of Colorado in partial fulfillment
of the requirements for the award of departmental honors in the Department of
Astrophysical and Planetary Sciences.*

Committee Members:

Advisor: Dr. Jack Burns, Dept. of Astrophysical and Planetary Sciences
Dr. Erica Ellingson, Dept. of Astrophysical and Planetary Sciences
Dr. Christine MacDonald, Dept. of Writing and Rhetoric
Dr. Raul Monsalve, Center for Astrophysics and Space Astronomy

April 12, 2017

University of Colorado at Boulder

Abstract

Astrophysical and Planetary Sciences

Statistical Modeling and Beam Parameterization of the Redshifted Global 21 Centimeter Signal

by Katherine June PELLICORE

This thesis explores two aspects of measurements of the global 21 cm signal through analytical simulations. We first attempt to understand how well the global 21 cm signal could be extracted from measurements of the sky. We accomplish this by employing a Fisher matrix analysis to estimate the uncertainties of cosmological parameters for simple measurement models that assume a perfectly calibrated instrument. We find that the assumed parameters of the signal can be constrained to high precision under realistic scenarios of noise and foreground contaminants. We also study the bias in the cosmological parameters due to modeling errors using a Fisher matrix approach. We find that for all cases studied, which correspond to simple frequency independent and frequency dependent model errors smaller than the global 21 cm signal, the bias is not significant. We then examine the spectral structure an instrument beam introduces in measurements of the global 21 cm signal. We simulate realistic beams that vary smoothly over frequency and space, and compute a beam-sky convolution to show how these beams interact with models of the sky. We find that beams that evolve linearly over the frequency range, as well as all bifurcating beams, introduce a spectral structure that is small enough to avoid obstructing measurements of the global 21 cm signal.

Acknowledgements

I would like to give my greatest thanks for this thesis to my mentor, Dr. Raul Monsalve. Although already overstretched and with more work on his plate than can be expected of any reasonable person, he devoted countless hours to this project, from assisting me with my coding problems to editing my thesis to trying to help me understand, for the thousandth time, the differences between various astronomical coordinate systems. Dr. Monsalve's guidance has helped me not only to develop my critical thinking and analysis skills, but also, perhaps more importantly, to look at the universe in ways I could have never imagined, and I will always look back on our various journeys to the Kalahari desert with fondness. My friends and family also deserve an enormous thank you for their tremendous and constant support. Without their unceasing pep talks, library snacks, and other sources of emotional/physical/inspirational support, I would have lost it long ago. In particular, I would like to thank my parents for being with me every step of the way since my very first day of school. I will forever be grateful to them for always believing in my capacity to accomplish whatever it was that I had decided to set out to do, and for always encouraging me to do my best and forget the rest. This thesis is for them. I would also like to express my gratitude to Rihanna's 2007 smash-hit *Disturbia* for getting me through some sad moments in the library and reminding me that, sometimes, the darkness really is the light. Finally, I would like to thank my advisor, Dr. Jack Burns, and the rest of my committee members for taking the time out of their busy schedules to read and review this thesis.

Contents

Abstract	iii
Acknowledgements	v
1 Introduction	1
1.1 The Hydrogen Spectral Line from the Early Universe	1
1.2 Thesis Overview	4
2 Implementation of Fisher Matrix Forecasting Code	5
2.1 Fisher Matrix and Confidence Ellipses	5
2.1.1 Motivation	5
2.1.2 Computation Method	6
2.2 Statistical Uncertainty in the Global 21 Cm Signal Model	7
2.2.1 Cosmological Signal Model	8
2.2.2 Foreground Models	8
2.2.3 Noise Model	11
2.2.4 Results	12
Case One	13
Case Two	15
Case Three	18
2.2.5 Discussion	20
2.3 Bias in the Global 21 Cm Signal Measurements	20
2.3.1 Bias Equation	21
2.3.2 Models	22
Measurement Models	22
Model Errors	22

2.3.3	Results and Discussion	23
2.4	Summary	26
3	Effects of Smoothly Varying Antenna Beams on Wideband Measurements of the Low-Frequency Sky	27
3.1	Measurement of the Sky Through an Antenna Beam	28
3.2	Sky Models	29
3.2.1	Scaled Haslam Map	29
3.2.2	Guzman-Haslam Interpolation	31
3.3	Beam Models	32
3.3.1	General Beam Equation	32
3.3.2	Circular Beam	33
3.3.3	Elliptical Beam	34
3.3.4	Bifurcating Beam	35
3.4	Details of Simulations	38
3.5	Results and Discussion	42
3.5.1	Comparisons of Antenna Temperatures	42
3.5.2	Polynomial Fitting of the Antenna Temperature	46
3.6	Summary	54
4	Summary and Future Work	55
5	Bibliography	57

Chapter 1

Introduction

1.1 The Hydrogen Spectral Line from the Early Universe

About 380,000 years after the Big Bang, photons decoupled from baryons, emitting the Cosmic Microwave Background. This left a transparent universe full of neutral hydrogen for millions of years. Slowly, more dense regions in the universe began to collapse until they started to produce the first generation of stars, supernovae, black holes, and quasars at about 100 million years after the Big Bang. Gradually, ultraviolet radiation from these first generations of compact sources ionized the hydrogen in the intergalactic medium. This era is of particular interest to cosmologists today because not much is known about the universe during these epochs of cosmic dawn and reionization. There is little concrete evidence surrounding the first ionizing objects, how much radiation they produced, or how reionization progressed.

The redshifted 21 centimeter signal from neutral hydrogen can be used to study the early universe. A neutral hydrogen atom in the ground state consists of one proton and one electron, each with their own magnetic dipole moment and spin. There is a slight increase in energy when the spins are parallel and a decrease in energy when they are antiparallel. When the electron and proton spins of a hydrogen atom change from parallel to antiparallel, energy is released and the atom emits a photon with a wavelength of 21 cm, which corresponds to a frequency of 1420 MHz. The intergalactic medium in the early universe consisted predominantly of neutral hydrogen, and thus current theoretical models predict that measuring the 21 cm signal is the most direct way of probing the large scale evolution of the universe as a

function of time [Furlanetto et al., 2006]. Features of the cosmological signal would provide information about properties of the first luminous objects, time line of reionization, and many other important aspects of the early universe that are unknown to cosmologists today.

The 21 cm cosmological signal has been redshifted, or stretched in wavelength, over time as a result of the expansion of the universe. Whenever a light source is moved away from an observer, a redshift occurs and the wavelength of the light increases while the frequency in turn decreases. Because the redshift, z , is a measurement of how the properties of light change as it moves with respect to an observer, it is directly related to frequency, as given by the following equation:

$$z = \frac{\nu_{em} - \nu_{obs}}{\nu_{obs}} \quad (1.1)$$

where ν_{em} is the frequency emitted by a light source and ν_{obs} is the frequency observed. As the universe expands over time, light moves away from an observer and creates a redshift that is related to the time since the Big Bang. The age of the universe today is defined to be at redshift zero, with redshift increasing as you move backwards in time. As a reference, Table 1.1 presents both the redshifts and the frequencies of the 21 cm cosmological signal that correspond to the time since the Big Bang.

Time [Myr]	Redshift	ν [MHz]
40	56	25
100	30	47
500	10	130
1000	6	200

TABLE 1.1: Time since the Big Bang and the corresponding redshifts and frequency of the 21 cm signal

The early universe has a high redshift, which corresponds to a lower frequency of the cosmological signal. Today, we expect most of the cosmological signal to be constrained within the frequency range of 40-120 MHz, which corresponds to a redshift range of 35-15. Though theory predicts the existence of the 21 cm signal

from the early universe, it has never been measured, and experiments over the last decade have all been unsuccessful in their attempts to extract it from the galactic foregrounds.

Most modern experiments use one of two instrumental methods to measure the cosmological signal in the low-frequency (MHz) radio sky: an interferometer array or a single antenna with a wide beam [Harker et al., 2012; Mozdzen et al., 2016; van Haarlem et al., 2013]. An interferometer array uses a collection of telescopes that simultaneously measure the sky temperature for higher resolution images. This measurement could show the spatial and redshift dependence of the cosmological signal and produce statistics and images of the brightness temperature over the whole sky. A single antenna measures the global, or sky averaged, 21 cm signal as a function of frequency and, therefore, redshift. This method cannot characterize the spatial resolution of the 21 cm signal, but it is capable, in principle, of providing an estimate of its monopole component. Using a single antenna is advantageous because it is both simpler and less expensive than using an interferometer array. The broad spectral features of the global signal trace the transitions of the intergalactic medium in the early universe. Models of the global signal show three main features, with an absorption trough as the strongest aspect of the signal. There are also two small features, one before and after the trough, corresponding to events during the Dark Ages and Epoch of Reionization, respectively. The 21 cm signal would have evolved with time until approximately redshift six, after which it disappears due to the reionization of the neutral hydrogen in the intergalactic medium. Figure 1.1 shows the features of the global 21 cm signal as a function of both frequency and redshift.

Measurements of the global signal produce an antenna temperature spectrum that is dominated by strong diffuse foregrounds. These foregrounds are about four orders of magnitude larger than the signal, making accurate measurements of the global signal very challenging. Although the foregrounds are strong, they are smooth in frequency, making it possible to extract the global 21 cm signal from measurements of the sky temperature [Harker et al., 2012].

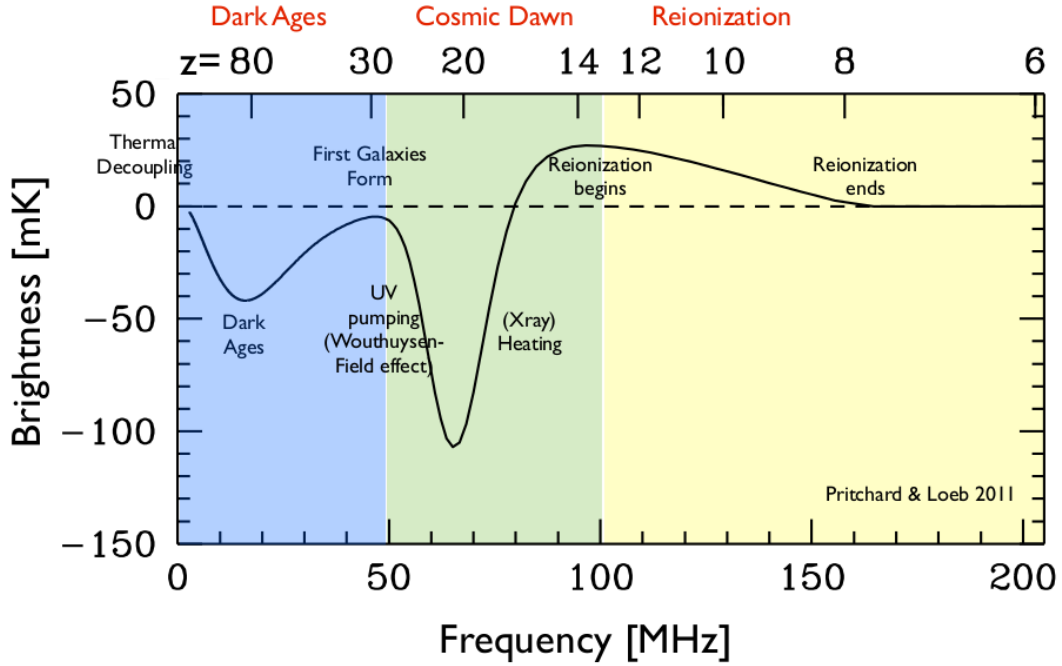


FIGURE 1.1: The spectral shape of the global 21 cm signal [Pritchard and Loeb, 2011]. The main feature is a central absorption trough, with two smaller features before and after the trough.

1.2 Thesis Overview

Using simulations, this thesis explores two important aspects of the global 21 cm signal which are relevant for instruments observing either from Earth or space. Chapter 2 explores an analytic method that contributes to the understanding of how well the global 21 cm signal can be extracted from measurements conducted under ideal conditions. Specifically, it describes the implementation of the Fisher matrix approach for estimating the uncertainties on parameters for a simple model of the global 21 cm signal under realistic scenarios of noise and foreground contamination. It also describes the use of a Fisher matrix approach to estimate biases in the parameters when the assumed model for the global 21 cm signal is incorrect. Chapter 3 studies an important instrumental aspect of this measurement. For an otherwise perfectly calibrated instrument, the frequency dependence of the antenna beam introduces spectral structure in measurements of the global 21 cm signal. We examine the properties of this structure for simple but realistic simulated beams with smooth frequency and spatial variations. Chapter 4 discusses and summarizes the key findings of this thesis.

Chapter 2

Implementation of Fisher Matrix Forecasting Code

Fisher matrices are a mathematical modeling tool to estimate uncertainties in model parameters for Gaussian measurement errors. Biases in the parameters due to incorrect models can also be estimated with this formalism. In this chapter, we model sky temperature spectrum in the range of 40 to 120 MHz, which corresponds to a redshift range of 35-15. We then explore the use of Fisher matrices to estimate uncertainties for parameters of simple models of the 21 cm signal.

2.1 Fisher Matrix and Confidence Ellipses

2.1.1 Motivation

Fisher matrices are used widely in astrophysical research to estimate parameter measurement uncertainties from measurement models [Pritchard and Loeb, 2010]. They are a practical tool for forecasting experimental uncertainties primarily because they represent a completely analytical method. The Fisher method allows us to use models for both the noise and the measurement, thus permitting accurate calculation of future measurement uncertainties without expensive simulations to produce synthetic data. After we compute the Fisher matrices, we can plot the results in the form of confidence ellipses in order to visually represent the uncertainties.

2.1.2 Computation Method

The Fisher matrix is computed using the equation:

$$F = J_{\lambda_0}^T \Sigma^{-1} J_{\lambda_0}. \quad (2.1)$$

First, we compute the Jacobian, J , of the measurement model. This is done by taking the derivative of the model with respect to each fit parameter. The Jacobian is then evaluated at the nominal value for each of the parameters, λ_0 . When the measurement is a frequency spectrum, this will produce an $N_\nu \times N_\lambda$ matrix, with N_ν representing the number of frequency channels and N_λ representing the number of parameters.

Eqn. 2.1 requires an equation for the covariance noise, Σ , computed using the noise models described below in Section 2.2.3. This is an $N_\nu \times N_\nu$ matrix.

The Fisher matrix has dimensions of $N_\lambda \times N_\lambda$. The uncertainties in the parameters are obtained by inverting the Fisher matrix, which creates an $N_\lambda \times N_\lambda$ parameter covariance matrix, C . The diagonal terms represent the variance of each parameter, and the cross terms represent the covariance between pairs of parameter uncertainties.

In this chapter, we compute the Jacobian using the measurement models described in Section 2.2. Our frequency range is from 40-120 MHz, and thus N_ν has 81 terms. We analyze measurement models with 3 to 8 fit parameters, and therefore the length of N_λ varies. We implemented these computations in Python using the SymPy module, which provides the capability of computing derivatives of analytical models and then evaluating them at specific values.

We visualize these uncertainties in the form of ellipses that represent constant probability limits in the uncertainty distribution. The ellipse dimensions are taken from the parameter covariance matrix. If we have two parameters, j and k , then they will have a covariance matrix:

$$F^{-1} = C = \begin{bmatrix} \sigma_j^2 & \sigma_{jk} \\ \sigma_{jk} & \sigma_k^2 \end{bmatrix}. \quad (2.2)$$

The semi-major axis a , semi-minor axis b , and rotation angle θ of the confidence ellipses are calculated as follows:

$$a^2 = \frac{\sigma_j^2 + \sigma_k^2}{2} + \sqrt{\frac{(\sigma_j^2 - \sigma_k^2)^2}{4} + \sigma_{jk}^2} \quad (2.3)$$

$$b^2 = \frac{\sigma_j^2 + \sigma_k^2}{2} - \sqrt{\frac{(\sigma_j^2 - \sigma_k^2)^2}{4} + \sigma_{jk}^2} \quad (2.4)$$

$$\tan 2\theta = \frac{2\sigma_{jk}}{\sigma_j^2 - \sigma_k^2} \quad (2.5)$$

These equations, as summarized from Coe, 2011, can be used to construct confidence ellipses for any $N_\lambda \times N_\lambda$ parameter covariance matrix. To get a constant probability limit, the width and the height of each ellipse must be multiplied by a scaling factor, α . For a 68.3% probability limit, α has a value of 1.52, and for 95.2% α is equal to 2.48.

2.2 Statistical Uncertainty in the Global 21 Cm Signal Model

We model the temperature spectrum over frequency, ν , assuming a perfectly calibrated instrument. Our measurement model contains contributions from the cosmological signal, diffuse foregrounds, and noise, i.e:

$$T_{sky} = T_{FG} + T_{21} + Noise \quad (2.6)$$

where T_{sky} is the sky temperature, T_{FG} is the foreground temperature, and T_{21} is the temperature of the global 21 cm signal. Our analysis assumes that we simultaneously fit a set of parameters for the global 21 cm and parameters for the foreground.

2.2.1 Cosmological Signal Model

We model the global 21 cm signal using a Gaussian:

$$T(A, \nu_0, FWHM; \nu) = Ae^{\frac{-4\ln(2)(\nu-\nu_0)^2}{FWHM^2}} \quad (2.7)$$

Given the uncertainties in predictions of the global 21 cm signal, current studies [Bernardi et al., 2015, 2016; Mozdzen et al., 2016] use expressions of this type as first order approximations. The fit parameters of this equation are the amplitude A , the full width at half maximum $FWHM$, and the center frequency ν_0 . These parameters and their nominal values are shown in Table 2.1.

Parameter	Description	Nominal Value
A	Amplitude	-100 mK
$FWHM$	Full Width at Half Maximum	20 MHz
ν_0	Centering Frequency	80 MHz

TABLE 2.1: Parameters and nominal values of the cosmological signal model.

Figure 2.1 shows the cosmological signal plotted across the frequency range. The key feature of the signal is the absorption trough, which is represented by this Gaussian model.

2.2.2 Foreground Models

The largest contribution to the spectrum in our frequency range is due to the diffuse emission from our galaxy [Bernardi et al., 2015; Harker et al., 2012]. The radiation mechanism for this signal is broadband synchrotron radiation, which arises from relativistic charged particles. When the particles encounter a strong magnetic field, they are accelerated and emit radio waves that contribute to about 75% of the total foreground intensity [Zaroubi, 2012], with the remaining fraction produced by the integrated effect of extragalactic point sources, in addition to other diffuse foregrounds such as free-free radiation.

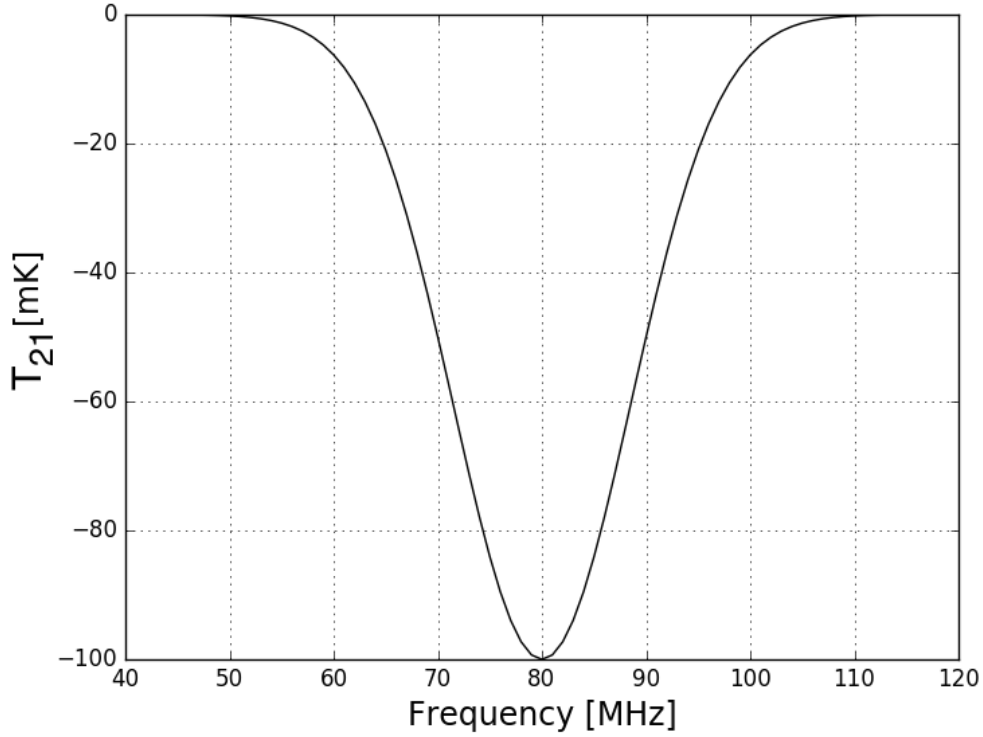


FIGURE 2.1: Temperature as a function of frequency for the Gaussian model of the global cosmological signal. The absorption trough of the signal has an amplitude of only -100 mK.

We consider two models that account for the foreground spectrum in this chapter. The first, from Bernardi et al., 2015, uses a single power law function, and is given by the equation:

$$T_{FG}(T_0, \beta; \nu) = T_0 \left(\frac{\nu}{\nu_n} \right)^\beta \quad (2.8)$$

The fit parameters in this model are the reference temperature, T_0 , at $\nu_n = 80$ MHz and the spectral index β . Their nominal values are shown in Table 2.2.

Parameter	Description	Nominal Value
T_0	Brightness Temperature	1000 K
β	Spectral Index	-2.5

TABLE 2.2: Parameters and nominal values for the first foreground model.

This model represents a first order approximation to a real foreground spectrum,

which, although smooth, would require more than a single spectral parameter [Mozdzen et al., 2017].

The second foreground model consists of a five-term polynomial. The galactic foregrounds do not follow an exact power law function, and thus need more than one term to be represented accurately. We use a model introduced in Mozdzen et al. 2016, which corresponds to a generic five-term polynomial scaled by a power law with β equal to -2.5:

$$T_{FG}(a_i; \nu) = \sum_{i=0}^4 a_i \nu^{-2.5+i} \quad (2.9)$$

The nominal values for the polynomial fit parameters are shown in Table 2.3, and were derived from a fit to a sky spectrum measured by the EDGES experiment in Western Australia [EDGES collaboration, 2017; in preparation].

Parameter	Description	Nominal Value
a_0	Polynomial	879.03948833 K
a_1	Polynomial	2887.92106234 K
a_2	Polynomial	-4348.12441145 K
a_3	Polynomial	2697.33157658 K
a_4	Polynomial	-564.14138205 K

TABLE 2.3: Parameters and nominal values for the fit amplitude parameters.

Figure 2.2 shows our second foreground model.

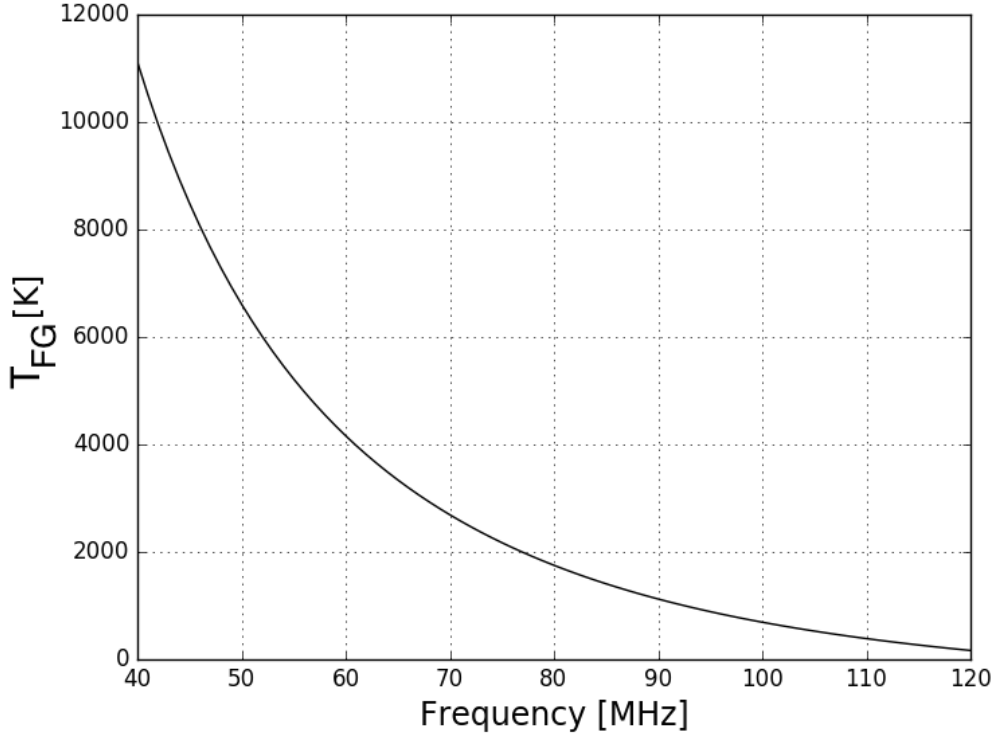


FIGURE 2.2: Model for the sky-average foreground temperature produced by fitting a real sky spectrum with the EDGES polynomial of Eqn. 2.9.

2.2.3 Noise Model

The measured noise in this type of experiment is proportional to the system temperature and dominated by the diffuse galactic foreground intensity, which has temperatures reaching thousands of Kelvin. Noise from the instrument is minor, with typical values below a few hundred Kelvin. This is represented by Eqn. 2.10:

$$T_{sys} = T_{FG} + T_{21} + T_{inst} \approx T_{FG} \quad (2.10)$$

We assume that integration of hundreds of hours has reduced the noise to levels below those of global 21 cm signal. Our noise model, as in Harker et al., 2012, corresponds to the radiometer equation, which assumes a frequency-dependent noise standard deviation proportional to the foreground temperature:

$$\sigma_{noise} = \frac{T_{FG}}{\sqrt{\Delta\nu\Delta t}} \quad (2.11)$$

In order to reduce the noise below the level of the 21 cm signal, we assume both a frequency channel width, $\Delta\nu$, of 1 MHz and that the observation is conducted over a period of Δt equal to 500 hours. Clearly, a larger value of either parameter reduces the measurement noise. Figure 2.3 shows the noise standard deviation derived from our model, as well as one random noise realization.

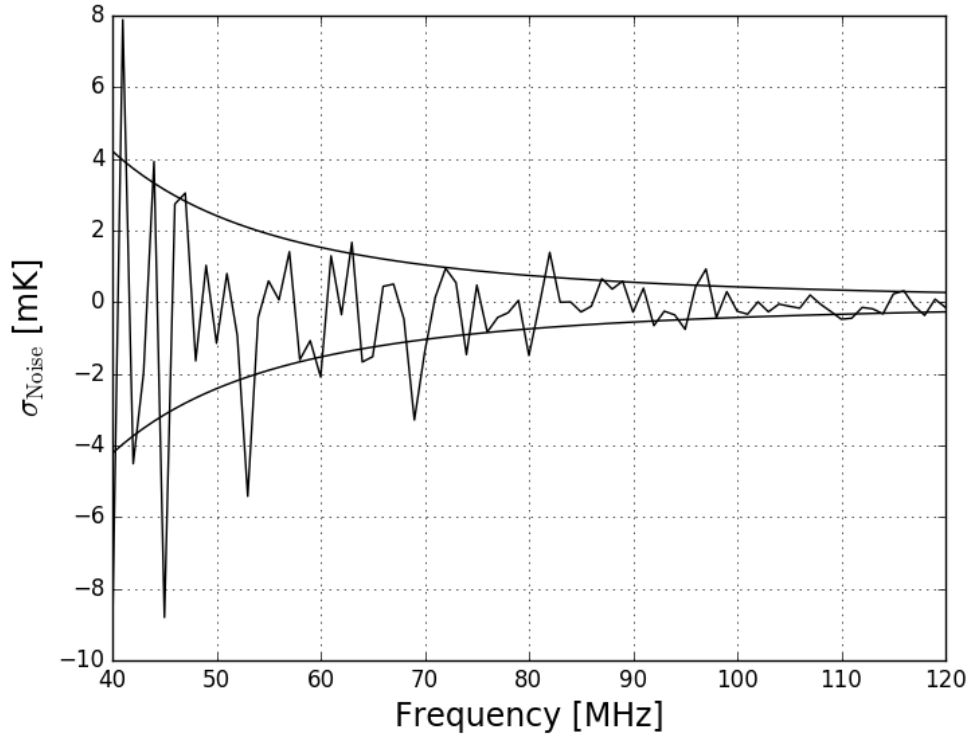


FIGURE 2.3: Noise our model for the in sky temperature as a function of frequency produced by the radiometer equation (Eqn. 2.12). The smooth lines represent the frequency-dependent standard deviation. In addition, we show one random noise realization for reference.

2.2.4 Results

From the Fisher matrices, we produced covariance matrices for the fit parameters in our simulated measurements consisting of the global 21 cm model, a foreground model, and the noise model.

We show the results of our uncertainty computations in the form of triangle plots that depict the covariances between pairs of fit parameters. These plots show ellipses for 68.3% and 95.4% confidence levels, represented by a blue and red line, respectively, on the plots. The black cross in the center of every ellipse represents the fiducial value of each parameter. Low covariance relationships correspond to either circular limits or elongated ellipses aligned with either the x or y axis. High correlation is depicted by an elongated ellipse not aligned with any axis. The width of an ellipse corresponds to its marginalized uncertainty. We show this marginalized uncertainty in the black at the top of each panel column.

Though the observing time has a fiducial value of 500 hours, we experimented with times ranging from 125 to 500 hours. Noise, and thus measurement uncertainty, increases with a shorter observing time, but the parameter uncertainties do not degrade significantly. Because of the square root in the denominator of the radiometer equation (Eqn. 2.11), doubling the observing time does not necessarily decrease the noise by a factor of two. For example, when computing the first foreground model (Eqn. 2.9) the uncertainty in the full width at half maximum increases by only 0.7% when the observing time is cut from 500 to 125 hours. Unless the observing time changes dramatically, this parameter has a minor and well-understood effect on measurement uncertainties, so we neglect any further analysis of this aspect for the remainder of this thesis.

Figure 2.4 shows the confidence ellipses and one dimensional Gaussian distributions for the three fit parameters in the cosmological signal model, Figure 2.5 displays ellipses for the foreground model with a single power law, and Figure 2.6 is the triangle plot for the five term foreground model. In all cases, the cosmological parameters (A , $FWHM$, ν_0) are the same.

Case One

The model in this case corresponds to the global 21 cm signal with no foregrounds. Although not physically realistic, we use this model as a baseline reference for the measurement uncertainties.

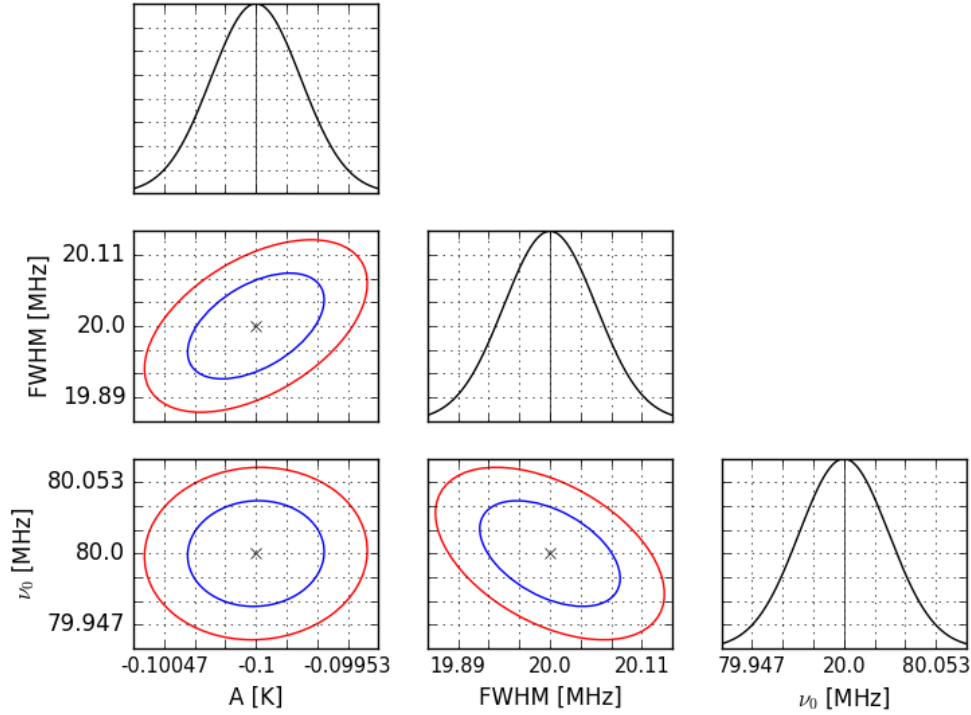


FIGURE 2.4: Case One: No Foregrounds. Confidence ellipses and normalized one-dimensional Gaussian distributions for the three parameters in the cosmological signal model. This case shows the smallest uncertainties for the three cosmological fit parameters.

We expect to see the smallest cosmological uncertainties in this model because of the lack of foregrounds and, consequently, the lower number of parameters. From the one-dimensional Gaussian distributions in black, we can indeed see that the uncertainties in the three cosmological parameters are very small, with 95.4% uncertainty limits to within 0.6% percent of the nominal values.

By examining the orientation of the ellipses, we can see that the ellipse of the amplitude of the signal, A , and the center of the Gaussian, ν_0 , is almost completely circular and aligned with the axis. There is therefore no correlation between these two parameters, which is to be expected because the shifts in ν_0 are orthogonal to the amplitude. We can analyze this quantitatively by computing the correlation coefficient between the two parameters, ρ , using the following equation:

$$\rho_{jk} = \frac{\sigma_{jk}}{\sigma_j \sigma_k} \quad (2.12)$$

For A and ν_0 , the correlation coefficient is 0.036, confirming that the two parameters have a low covariance.

On the contrary, there are clear correlations between the other parameter pairs. For the case between ν_0 and the full width at half maximum, this occurs because small changes in the Gaussian center due to measurement uncertainties causes confusion with changes in its width. In other words, ν_0 and the full width at half maximum are not orthogonal to each other, which produces their covariance. Similarly, changes in the full width at half maximum of the Gaussian easily affect its amplitude, and because these parameters are not orthogonal they will have non-zero covariances.

These observations are reflected in the correlation coefficient, ρ , between the parameter pairs. A and the *FWHM* have a correlation coefficient with a magnitude of 0.49, which is almost fourteen times larger than the correlation between A and ν_0 . The correlation coefficient for the *FWHM* and ν_0 , is similarly large and has a magnitude of 0.47, which is thirteen times larger than that between A and ν_0 .

Case Two

The triangle plot for Case Two was constructed using the cosmological signal model and the power law function (Eqn. 2.8) as the foreground model. Though there are a number of interesting features in the triangle plot of Case Two, we highlight only a few in this section.

We expect the incorporation of the foreground in the measurement model to increase the uncertainties in the three cosmological fit parameters. Examination of Figure 2.5 confirms this expectation. We analyze this quantitatively by examining the one-dimensional Gaussian distributions for Case Two as compared to Case One. The $1\text{-}\sigma$ uncertainty (68.3% confidence level) increased from Case 1 by 8.6% for the amplitude A , 19.9% for the *FWHM*, and 5.9% for the center frequency ν_0 . Although the uncertainties in all three cosmological parameters have increased, they are still notably small; at a 95.4% confidence level they are within 0.8% of the nominal values.

The ellipse showing the covariance of the *FWHM* and T_0 depicts one of the highest ellipticities for Case 2. This is because small parameter variations are not orthogonal

and have a positive correlation. A positive correlation implies that as T_0 increases, the *FWHM* tends to be estimated as larger values than its true value, for a given noise level. The correlation coefficient, ρ , between these two parameters is 0.56, confirming this observation.

The correlation between the three cosmological parameters (A , ν_0 , and the *FWHM*) have generally increased, with the exception of the correlation between the *FWHM* and the amplitude. The addition of the foreground term weakens the effect of a changing amplitude on the uncertainty of the full width at half maximum, and thus a decrease in ρ is to be expected for these two parameters.

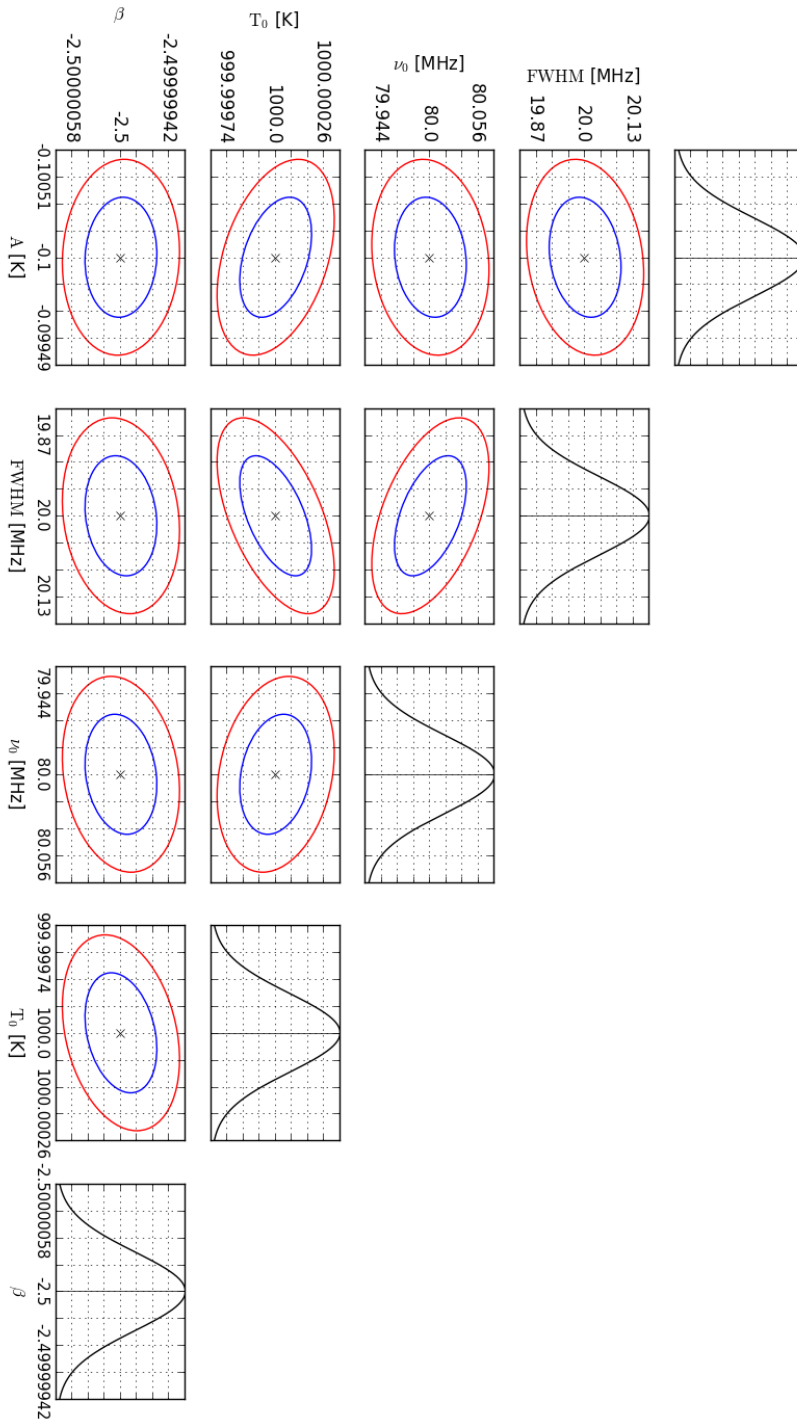


FIGURE 2.5: Confidence ellipses and normalized one-dimensional Gaussian distributions for the five parameters in the model of Case Two.

Case Three

Case Three corresponds to a five-term polynomial model of the foreground. By examining the size of the confidence ellipses in Figure 2.6, we can see that this model produces the largest uncertainties of the three cases.

To see this quantitatively, we can look at the covariance matrices for each of the three triangle plots. For example, the uncertainty in A increases by a factor of 4.5 from Case One to Case Three. The uncertainty in ν_0 is the most stable of the three and only increases by 70% from Case One to Case Three. These increases result from the higher number of parameters. Although the total uncertainties on each parameter increased in Case Three, the uncertainties on the cosmological parameters are still well-constrained, with 95.4% confidence within 2% of the nominal values of A , the full width at half maximum, and ν_0 .

The polynomial model also introduces the largest covariance between pairs of parameters, as evidenced both by how much narrower the confidence ellipses are in Figure 2.6 than the other plots and by the correlation coefficient, ρ . This is typical behavior for polynomials, and is to be expected. As an example, the correlation coefficient between a_0 and a_1 is 0.27. The correlation between polynomial terms also changes direction depending on the degree of the polynomial terms, which is also typical behavior for polynomials.

The correlation between the three cosmological parameters increased for all cosmological parameters in Case Three. The correlation coefficient ρ between the amplitude A and the $FWHM$ has a magnitude of 0.89 and almost doubled between Case One and Case Three. ρ between A and ν_0 increased to 0.69 from 0.13 in Case Two and 0.036 in Case One. The correlation coefficient between the full width at half maximum and ν_0 increased by a factor of 1.6 from Case Two to Case Three.

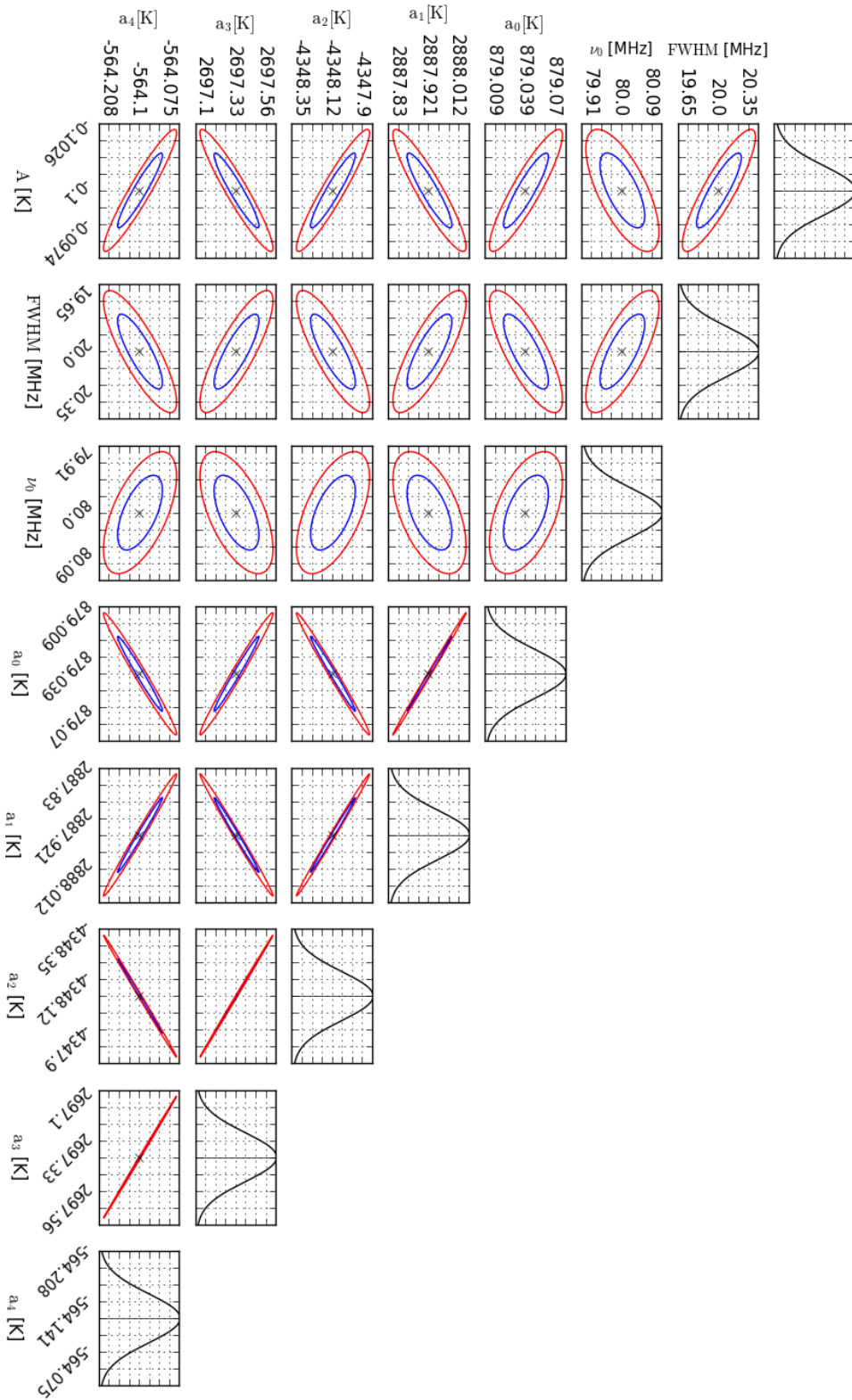


FIGURE 2.6: Confidence ellipses and normalized Gaussian distributions for Case Three, which models the foreground as a five-term polynomial.

2.2.5 Discussion

We found that additional parameters in the measurement model increase the uncertainty as well as the covariance between the cosmological parameters of interest. This is because by adding extra free parameters we are also assuming the uncertainty in that parameter and its effects on the others. This is particularly relevant in the case where the model contains several polynomial terms of different order whose coefficients are mathematically unconstrained. Although the uncertainties grow as the foreground model becomes more complex, with measurement noise assumed with the radiometer equation, the uncertainties in the cosmological parameters are still small in the three cases (no foreground, simple power law, polynomial), and are constrained within 2% of the nominal value for even the most complex foreground models.

The results of these simulations have shown that low measurement noise corresponding to up to 500 hours of effective integration can result in low uncertainties in the cosmological parameters for a simple Gaussian cosmological signal model when observing low foregrounds that are spectrally smooth, modeled with up to five terms, and have no priors. This is valid under the assumption that the models are correct but could be generalized to imperfect but sufficiently accurate models. This Fisher matrix analysis can be extended to increasingly more complicated models with additional parameters for both the cosmological signal and the foregrounds. As the models become more accurate, the assumption of a perfect model will be justified, and therefore these predicted statistical uncertainties will become more representative of reality. We leave this analysis of more realistic models for future work.

2.3 Bias in the Global 21 Cm Signal Measurements

In the computation of the Fisher matrices and subsequent confidence ellipses, it was assumed that our measurement model was correct. This assumption may not be valid, so in this section we use an extension of the Fisher matrix approach to estimate

the bias in cosmological parameters for certain cases of model inaccuracies. This approach is still not widely used in experimental astrophysical research due to the increasing popularity of more mathematically rigorous methods such as Markov Chain Monte Carlo techniques [Harker et al., 2012]. However, as long as we have access to an analytical model for the measurement, the Fisher matrix approach is significantly less expensive computationally and produces results more quickly. We do not incorporate foregrounds in this analysis to focus on understanding the Fisher matrix results for a simple mathematical model with closed analytical bias solutions. We compare our results with analytical predictions for validation.

2.3.1 Bias Equation

Parameter bias corresponds to the difference between the true input parameter value and the value estimated after assuming an incorrect model. In the Fisher matrix approach, assuming that the biases are comparable to the statistical uncertainties, the bias in parameter i in the context of a global sky measurement is computed as in Bernardi et al., 2015, as:

$$Bias_i = \sum_{j=1}^{N_{par}} F_{ij}^{-1} \sum_{n=1}^{N_{chan}} \frac{1}{\sigma_{noise}^2} \frac{dT_{sky}(\nu_n)}{d\lambda_j} R(\nu_n) \quad (2.13)$$

The bias in parameter i is calculated by first taking the derivative of the measurement model with respect to each parameter and dividing by the channel variance. This is then multiplied by the model error, R . After summing over frequency channels and multiplying by the i th column of the Fisher matrix, we get a single number corresponding to the parameter bias.

In general, the bias on a parameter is significant when it is several times larger than its statistical uncertainty.

2.3.2 Models

Measurement Models

We computed the bias for the fit parameters in our Gaussian cosmological signal model (Eqn. 2.7) for two cases of model errors and frequency independent noise with a standard deviation of 1 mK.

Model Errors

We considered two types of errors in our Gaussian cosmological model. Both types were chosen because we can easily predict their effects and compare them with Fisher Matrix results.

The first type of model error is a frequency-independent offset, meaning R is a single number. As the model error increases, the bias in the amplitude, A , will correspondingly increase. As the amplitude changes, the position in of the full width at half maximum also changes, and thus the bias in that parameter increases. For this model error, we expect no bias in the center frequency because the error is orthogonal to the perturbation in ν_0 . The second model error we considered corresponds to a scaled version of the Gaussian cosmological model. We chose this error type because it again allows us to easily anticipate what the parameters should be. In particular, as the model error increases the bias in A will correspondingly increase in magnitude. However, because the model error corresponds to a Gaussian offset, the bias in ν_0 and the full width at half maximum will be zero.

The residual models for this section are "toy" models. Much like the cosmological signal model, they are not physically motivated. However, knowing how the bias should change in these two cases represents a reference for verification of the implementation of this Fisher matrix method for bias computation.

2.3.3 Results and Discussion

The bias for the frequency independent model error was computed for ten values of this error spaced linearly between 1 and 10 mK. Figure 2.7 shows how the bias in the three fit parameters varies as a function of value. As expected, the bias in ν_0 is zero for all model error values.

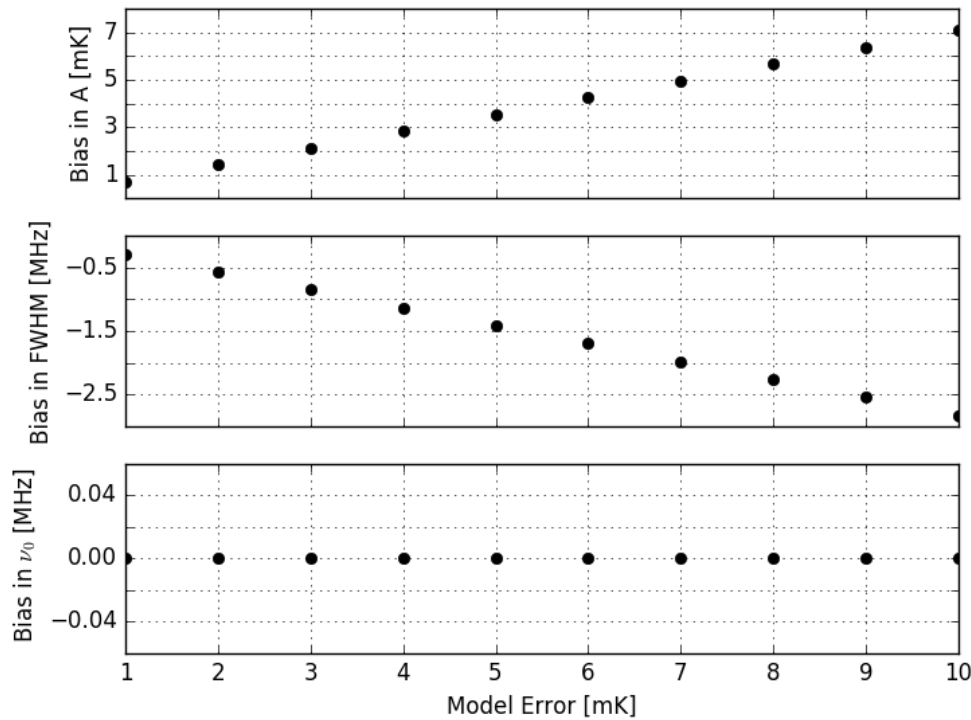


FIGURE 2.7: Bias in the three cosmological fit parameters for a frequency independent model error.

The correlation between the model error and the amplitude A is positive because the error makes the Gaussian appear smaller (less negative) relative to its nominal model with an amplitude of -100 mK. For a model error of 10 mK, the bias in A is 7 mK. The values for the error and the bias are not the same because, when affected by the error, the cosmological signal model is not a pure Gaussian anymore. This difference gets absorbed by more than one parameter. The full width at half maximum and the model error have a negative correlation because the error makes the Gaussian appear thinner compared to its nominal model; thus, as the model error increases the bias becomes more negative. For a model error of 1 mK, the bias in the FWHM is -0.28, and decreases to -2.8 for a model error of 10 mK.

Figure 2.8 shows the bias in the three fit parameters of the Gaussian model error with an amplitude that ranges from 1 to 10 mK. In this case, we only expect a bias in the amplitude. The results match this expectation. As in the previous case, the correlation between the bias in the amplitude and the model error is positive. For a Gaussian model error, the bias is exactly equal to the error. This shows the bias fully absorbs the model error, which matches the spectral shape of the cosmological signal. Specifically, when the Gaussian model error in the amplitude is 1 mK, the bias is 1 mK, and when the model error is 10 mK, the bias increases to 10 mK.

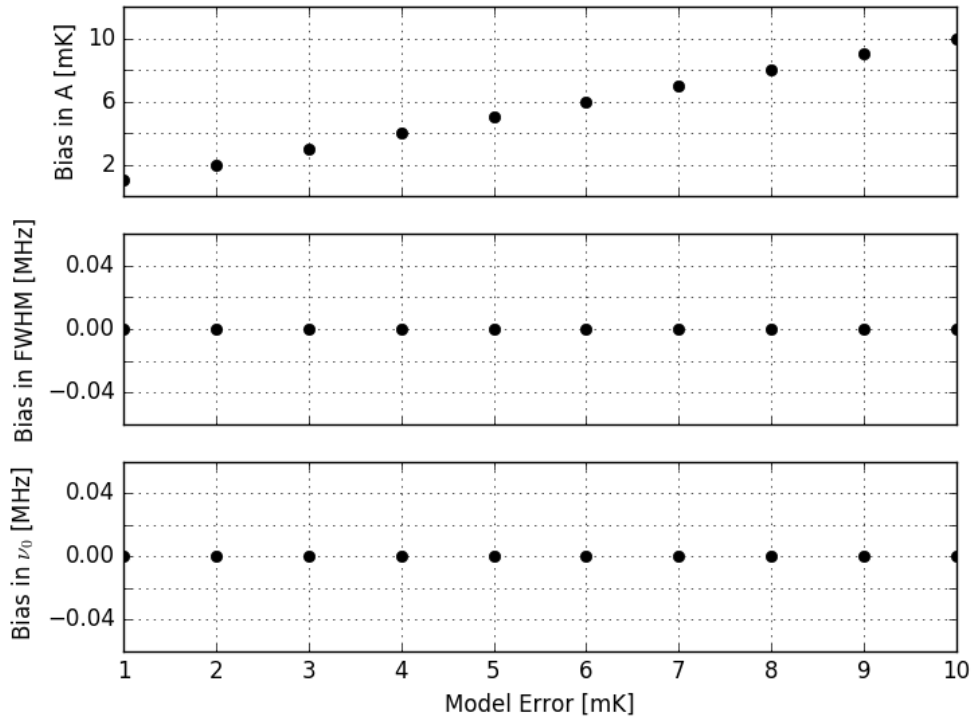


FIGURE 2.8: Bias in the three cosmological parameters for a Gaussian model error.

We complement the information in these two figures by showing triangle plots in Figures 2.9 and 2.10. These include the confidence ellipses due to the simulated statistical uncertainty, i.e. frequency independent noise with a standard deviation of 1 mK. The triangle plots include the location of the biased parameters, represented by a red circle, after a model error amplitude of 0.01 K, or 10 mK.

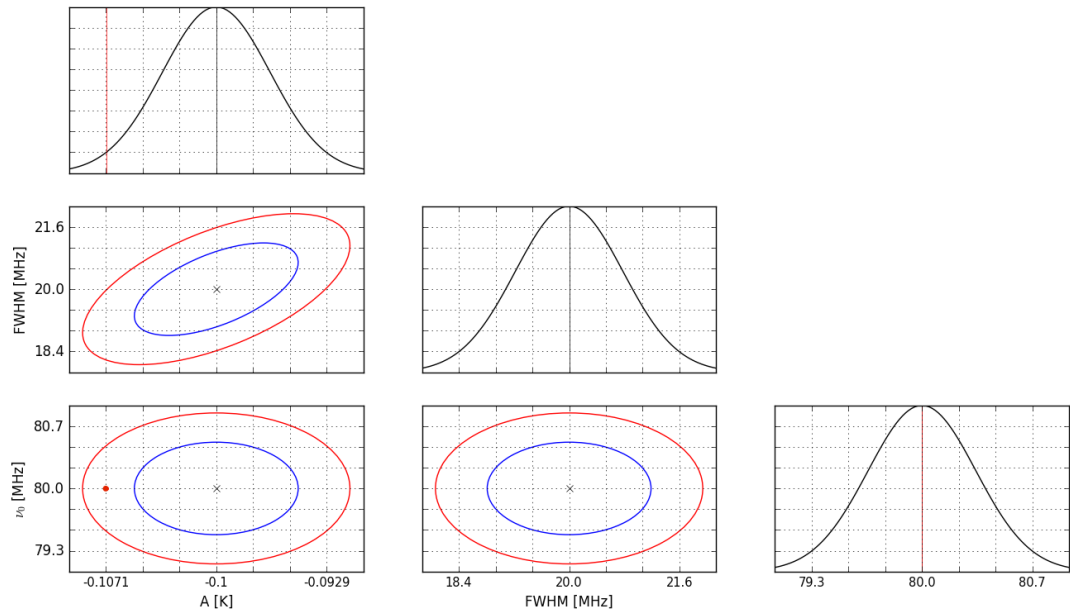


FIGURE 2.9: Confidence ellipses and normalized Gaussian distributions for a frequency-independent model error. The bias in the $FWHM$ is 4.4 times larger than the 68.3% confidence limits.

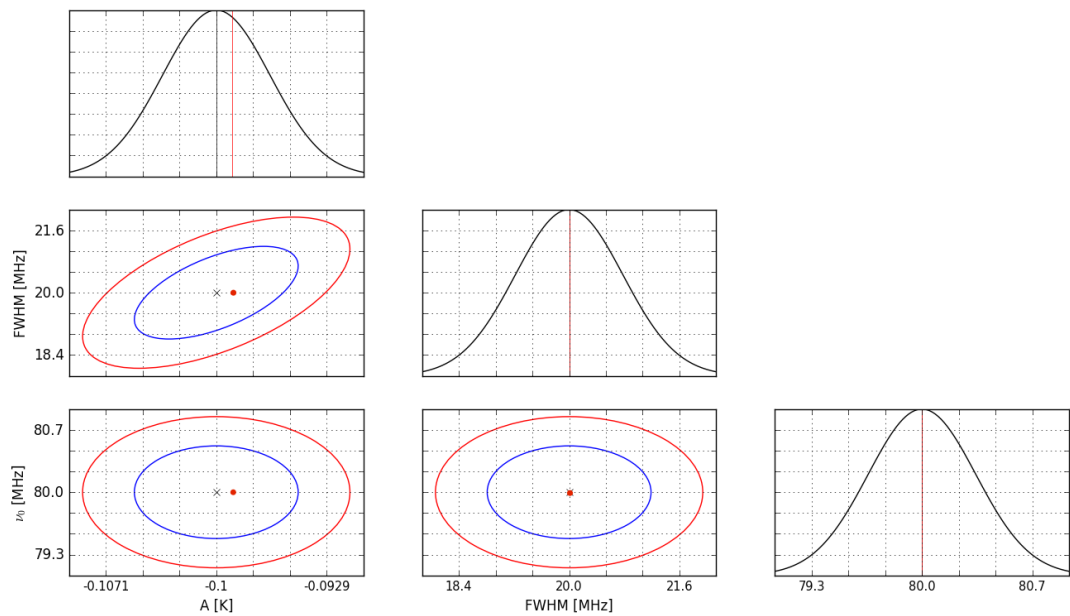


FIGURE 2.10: Confidence ellipses and normalized Gaussian distributions for a frequency-dependent Gaussian model error. As expected, the bias is nonzero only in the amplitude A .

We observe that the biases computed are comparable to the statistical uncertainty

resulting from our assumed noise level. The largest bias relative to the statistical uncertainty of the parameter occurs for the *FWHM* and a frequency independent model error. The ratio between the bias in the *FWHM* and its uncertainty from the covariance matrix has a magnitude of 4.4, which, although larger than in the other cases where the biases are constrained within the 95.4% confidence limits, is still in the limits of significance. More context would be required in order to definitively label the bias in the *FWHM* as significant for this assumed measurement uncertainty. Overall, all biases computed were constrained within 15% of the nominal value for each parameter for even the highest model errors.

The techniques used in this section can be used for further study of how the residuals affect measurement of the cosmological signal. The bias can be computed using the methods described in Section 2.4.1 for residuals that are out of the scope of this project, and future measurement attempts of the 21 cm signal use the results of this section as a reference point for their bias expectation values.

2.4 Summary

In this chapter we implemented a Fisher matrix method to estimate parameter uncertainty for a Gaussian model of the 21 cm cosmological signal. We forecasted measurement uncertainty using frequency dependent noise and two different foreground models. We found that as parameters are added to the foreground model, the uncertainties in the three fit parameters (A , the full width at half maximum, and ν_0) of the Gaussian grow. The bias, which quantifies parameter errors due to model error, was also computed using a Fisher matrix formalism. We found that, for the assumed frequency independent measured noise, the bias for all parameters was within an acceptable range, with less than a 15% change, of the computed statistical uncertainties.

Though the measurement models used in this chapter are not physically realistic, the Fisher matrix analysis for both the parameter uncertainties and the bias in each parameter can be used for future studies involving increasingly more complex models.

Chapter 3

Effects of Smoothly Varying Antenna Beams on Wideband Measurements of the Low-Frequency Sky

In order to precisely determine the global 21 cm signal, it is necessary to know the properties of the measurement instrument. Currently, the uncertainty of real experiments conducting this measurement is dominated by uncertainties in the instrument bandpass [Bernardi et al., 2015]. In turn, a significant contribution to this uncertainty arises from imperfect knowledge of the antenna beam. One of the ways this can be mitigated is by utilizing beams that do not vary significantly as a function of frequency. Sharp variations of a beam with frequency will result in sharp structure being introduced to the sky spectrum, which complicates the extraction of the cosmological signal [Mozdzen et al., 2016]. In the case of the global 21 cm measurement, all the cosmological information is contained in the spectrum. Therefore, it is critical to determine with precision the spectral properties of the antenna beam in order to remove them from the measurement. It is also important to conduct observations with beams that have minimal variations by design.

In this chapter, we evaluate the spectral contribution of smoothly varying antenna

beams produced from analytical models. Our computations described in this chapter can correspond to an instrument located either on Earth or in space. The key properties of our simulated beams, which include smooth spatial and spectral variance, are realistic to first order. We compute synthetic sky spectra by modeling observations of these beams pointing at low-foreground regions of a simulated radio sky. We analyze the results first by computing the difference between synthetic spectrum and a nominal spectrum that is generated using a frequency-independent beam. We then quantify the spectral structure of antenna temperature by fitting and removing a log-log polynomial to our beam-sky convolutions. An ideal beam would produce minimal spectral structure, but because realistic beams introduce chromatic, or frequency-dependent, effects that corrupt the beam [Mozdzen et al., 2016], it is critical to thoroughly understand the structure that an instrument introduces to measurements of the global 21 cm signal. Insufficient knowledge of the beam could lead to experimentalists incorrectly claiming a detection of the cosmological signal, because the spectral structure of the instrument could mimic sky spectrum variations from the global 21 cm signal [Harker et al., 2012].

3.1 Measurement of the Sky Through an Antenna Beam

An antenna beam describes the amplitude, or gain, of the antenna response to incoming radiation from all angles. This definition is valid for both a receiving and transmitting antenna. As an analogy, the antenna beam is equivalent to the space-dependent response of a microphone to incoming sound waves from all directions. Similarly, the signal produced at the terminals of a receiving antenna is the sum of the incoming radiation weighted by the antenna beam amplitude at each angle.

When an antenna beam points at the sky, the signal produced by the antenna, called antenna temperature, is given from Mozdzen et al., 2016 by:

$$T_A(\nu) = \frac{\sum_{\Omega} B(\hat{n}, \Omega, \nu) T_{Sky}(\Omega, \nu)}{\sum_{\Omega} B(\hat{n}, \Omega, \nu)} \quad (3.1)$$

where T_A represents antenna temperature, Ω represents spatial coordinates, \hat{n} represents the pointing coordinates, B represents the beam, and T_{Sky} represents intrinsic sky temperature. This calculation produces an antenna temperature in the same units as sky temperature, which has traditional units of Kelvin. From this calculation, it is clear that the frequency dependence of the beam can introduce structure in the antenna temperature spectrum that departs from the inherent frequency variations of the sky.

3.2 Sky Models

In this section, we describe the sky models used to compute the beam-sky convolution (Eqn. 3.1).

3.2.1 Scaled Haslam Map

The Haslam map is an all-sky map of diffuse emission at 408 MHz [Haslam et al., 1982]. The strongest contribution to the intensity in the map is Galactic synchrotron radiation. The Haslam map is widely used for simulations of observations by scaling it to the relevant frequency range using a power law spectral model. We obtain the map from the LAMBDA data sets accessed through the NASA Goddard Flight Center in HEALPix coordinates, with an NSide resolution of 512. For faster computation, we reduced this to NSide 64, which decreased the number of pixels by a factor of 64. Since we are interested in the range of frequencies from 40-120 MHz, the Haslam map is scaled to these frequencies as in Mozdzen et al., 2016, using the equation:

$$T_{sky} = T_{CMB} + (T_{408} - T_{CMB}) \left(\frac{\nu}{408} \right)^{-\beta} \quad (3.2)$$

where T_{408} is the original value of the Haslam map at 408 MHz at a given point, ν is the frequency range, β is the spectral index, and T_{CMB} is the temperature of the Cosmic Microwave Background and has a value of 2.725 K. The Haslam map is

originally represented in Galactic coordinates, but for our computations of antenna temperature with Eqn. 3.1 we must convert it to antenna-centered local coordinates. Galactic coordinates have their origin at the Galactic Center. Galactic longitude is analogous to terrestrial longitude, and is defined with its origin through the Galactic Center. Constant Galactic latitude lines are perpendicular to longitude, and parallel to the Galactic plane at Galactic latitude zero. Antenna-centered local coordinates are defined relative to the antenna itself. The azimuth varies between 0° and 360° on the plane perpendicular to the pointing direction. The elevation is defined parallel to the pointing direction, and has coordinate values ranging between -90° and 90° , with 90° being the elevation of the pointing coordinates. This elevation typically overlaps with the angle of highest antenna gain. Later computations in this chapter will be in equatorial coordinates, which have the heavens projected onto a sphere that encircles the Earth. This system is described using declination and right ascension. Declination is analogous to latitude, and is defined as the distance of an object from the equator, with values ranging from $\pm 90^\circ$. Right ascension is analogous to longitude, and is defined as how eastward an object is from the Vernal Equinox point. Right ascension is measured in hours, and passes through 360 degrees in 24 hours.

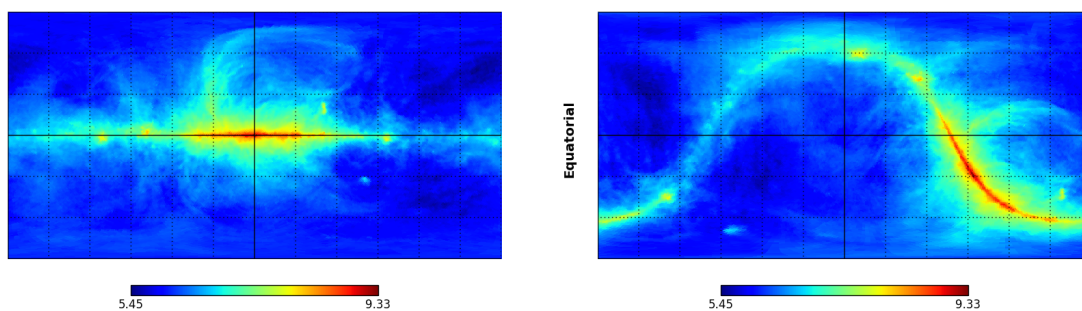


FIGURE 3.1: The log of the Haslam map in galactic coordinates on the left and equatorial coordinates on the right. The color scale represents the log of T_{Sky} in Kelvin, and the center of both maps represents the origin of each coordinate system. The area enclosed by each grid on the map denotes a 30° by 30° area.

3.2.2 Guzman-Haslam Interpolation

To model low-frequency observations, traditionally the spectral index β has been assumed to have a value of 2.5 that is constant across space. We compute a more realistic, spatially dependent β using two reference maps: the previously introduced Haslam map at 408 MHz and the Guzman map at 45 MHz [Guzman et al., 2011]. With these two maps at hand, the spectral index is computed as in Mozdzen et al., 2017 as:

$$\beta(\Omega) = \frac{\text{Log} \left(\frac{T_{45}(\Omega)}{T_{408}(\Omega)} \right)}{\text{Log} \left(\frac{45}{408} \right)} \quad (3.3)$$

where T_{45} is the Haslam 45 MHz map from section 3.2.1, and T_{408} is the Guzman 45 MHz sky map. In Mozdzen et al., 2017, they found that a sky model produced with this spatially dependent spectral index produces the best match to measurements of diffuse foregrounds to date. Figure 3.2 shows how the spatial dependence of our β computed with two maps.

To implement the Guzman-Haslam interpolation sky model, we scale the Haslam map using Eqn. 3.2 and transform it to local coordinates as in Section 3.2.1. In this case, though, we use our spatially variant β to compute the sky temperature.

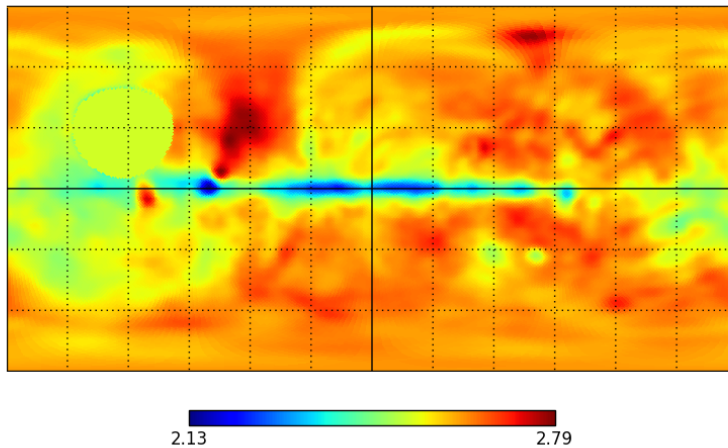


FIGURE 3.2: The spatially dependent spectral index β obtained by the Guzman-Haslam interpolation. The area enclosed by each grid represents a 30° by 30° area.

Because the Guzman-Haslam interpolation models the diffuse Galactic foregrounds much more accurately than the Haslam map, we use this sky model exclusively for our computations of the beam-sky convolution.

3.3 Beam Models

We study the effect of spectral properties in three Gaussian beams that, in terms of their spatial characteristics, we describe as circular, elliptical and bifurcating. A bifurcating beam is based on a circular Gaussian, and so also introduces ellipticity. Thus, it is the most general beam of the three. Moreover, it is also the beam type that most closely matches real wide antenna beams.

3.3.1 General Beam Equation

We constructed a single beam equation to model the three beam types. It is given by:

$$B(AZ, EL, \nu) = A_b[\cos(2[AZ - \phi_1]) + 1]B_n(EL) + Ae^{\frac{(EL-90)^2}{2\alpha^2}} \quad (3.4)$$

where

$$\alpha = \sqrt{\frac{F_x^2 F_y^2}{16 \ln(2)[F_x^2 \sin^2(AZ - \phi_0) + F_y^2 \cos^2(AZ - \phi_0)]}}. \quad (3.5)$$

The parameters in the beam equation and their significance are denoted in the table below:

Parameter	Description
EL	Elevation
AZ	Azimuth
A_b	Bifurcation Amplitude
A	Gaussian Beam Amplitude
ϕ_0	Elliptical Rotation Angle
ϕ_1	Bifurcating Rotation Angle
B_n	Bifurcating Function
F_x	FWHM in x
F_y	FWHM in y

TABLE 3.1: Table showing the parameters of the beam equation (Eqns. 3.4 and 3.5).

The bifurcation amplitude (A_b), Gaussian beam amplitude (A), and the two beam widths (F_x and F_y) can vary over the frequency range between predetermined minimum and maximum values. These spectrally dependent parameters can change either 1) linearly with a positive slope, 2) linearly with a negative slope, 3) quadratically with a positive slope, or 4) quadratically with a negative slope. A parameter that changes with a positive slope will be equal to its minimum value at 40 MHz and increase to its maximum value by the end of the frequency range, at 120 MHz. The two rotation angles, ϕ_0 and ϕ_1 , control the azimuthal offset of the beam and will have one of two values: 0° or 90° . The two beam full widths at half maximum, F_x and F_y , are defined perpendicular to each other. F_x is aligned with ϕ_0 , and thus, regardless of the beam's orientation, F_x will point in the same direction as ϕ_0 .

In the simulations, we compute the antenna temperature by varying only one beam parameter at a time over frequency while other variables in the beam equation are kept constant. By isolating each parameter, we can see how its frequency evolution uniquely affects the antenna temperature spectrum.

3.3.2 Circular Beam

A Gaussian circular beam is our simplest model of an antenna beam. It is an azimuthally symmetric beam and will therefore have constant gain at a given elevation. To produce a circular beam, the first term in the beam equation is dropped and

the two beam widths (F_x and F_y) are set equal to each other, so that α in the exponential of the beam equation is equal to a single value of $FWHM$. For this beam type, the full width at half maximum and the amplitude A can independently evolve over the frequency range as described above.

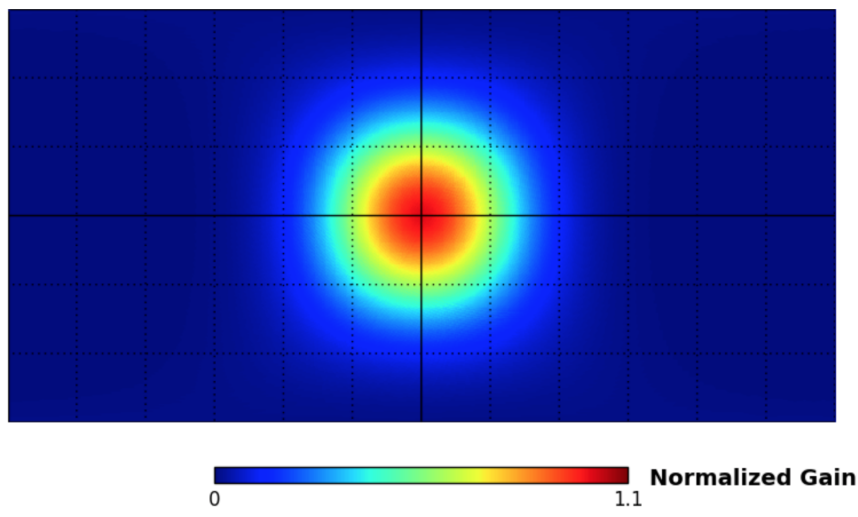


FIGURE 3.3: Normalized gain of a circular beam. The beam is shown projected onto equatorial coordinates with color representing gain and the area enclosed by each grid represents a 30° by 30° area.

Figures 3.3 and 3.4 show two depictions of the gain for a Gaussian circular beam. Figure 3.3 shows the normalized gain of a circular beam projected onto the sky in equatorial coordinates. Figure 3.4 is a scatter plot of the gain across azimuth and elevation, where the color of the pixels corresponds to the gain. Clearly, at a given elevation, the gain is constant across azimuth.

3.3.3 Elliptical Beam

For the elliptical beam, we once again drop the first term in the beam equation. This time, though, the F_x and F_y have different values, which results in α varying as a function of azimuth, generating ellipticity. Because an elliptical beam is no longer symmetric, gain is not uniform for a given pointing; the gain will be higher at some azimuths than others. F_x and F_y are spectrally variant over the frequency range, and the ratio of the two can either be locked or change over frequency. A locked ratio signifies that the ellipticity does not change over the frequency band, whereas an ellipse with an unlocked ratio changes proportions as it evolves in frequency. ϕ_0

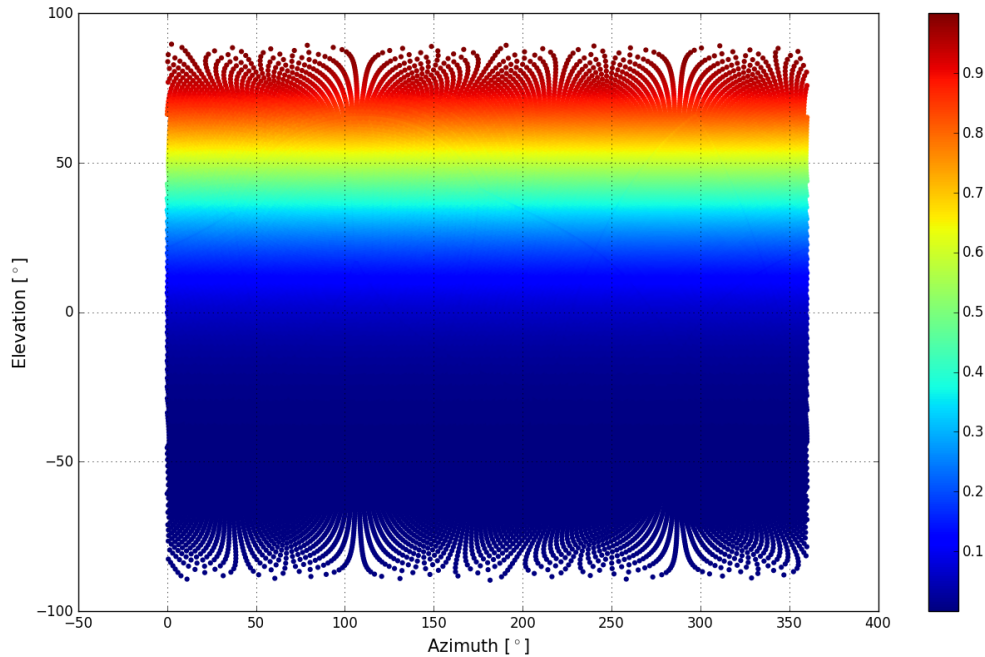


FIGURE 3.4: Normalized gain of a circular beam shown in antenna-centered local coordinates. At a constant elevation, the gain of a circular Gaussian beam is constant over azimuth.

controls the orientation of the beam, and has the option to change over angle to have a value of either 0° or 90° .

Figures 3.5 and 3.6 shows the same type of plots as Figures 3.3 and 3.4, but for an elliptical Gaussian beam with an azimuth offset of 0° and the F_y greater than the F_x . The projection of the beam in the Figure 3.5 has taken on an elliptical shape, the effects of which are evident in Figure 3.6, as the gain is no longer constant at a given elevation.

3.3.4 Bifurcating Beam

A bifurcating beam has equal full widths at half maximum in x and y , so that the Gaussian component of the beam equation is once again circular. However, the first term, which produces bifurcation in the beam equation, does not drop out in this case. This bifurcating term causes the gain to reach its highest value at two spatially different places, and then descend smoothly around each peak. These two definite

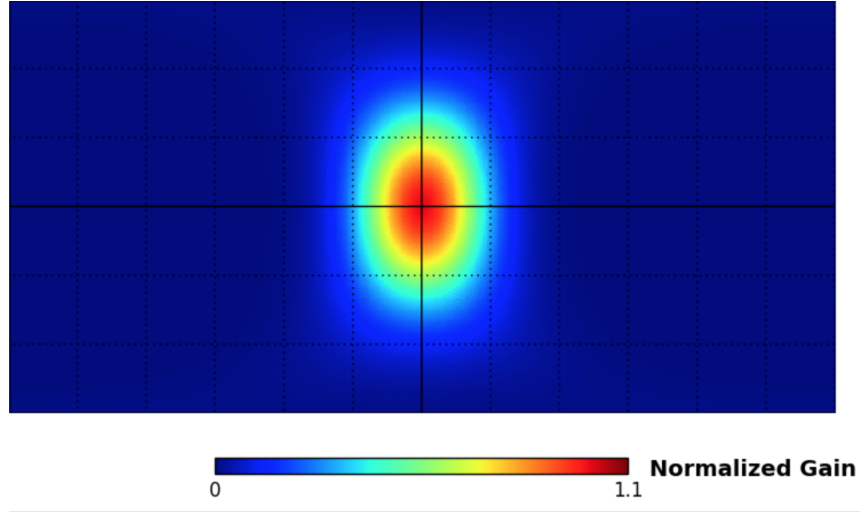


FIGURE 3.5: Gain of an elliptical beam projected onto equatorial coordinates, with the area enclosed by each grid representing a 30° by 30° area.

spikes in a bifurcating beam lead to considerable differences in gain at a given elevation.

We introduced the bifurcation through B_n , by defining it as follows:

$$B_n(EL) = \frac{1}{\Gamma\theta^\kappa} (90 - EL)^{\kappa-1} e^{-\frac{(90-EL)}{\theta}} \quad (3.6)$$

where Γ is the Gamma distribution parameterized by two numbers: the shape κ and the scale θ . We assign constant values of 7 for the shape and 3.5 for the scale. After B_n is computed, we normalize it and then multiply it to the the first term in the beam equation to obtain the bifurcation profile. For a Gaussian amplitude of $A = 1$, we let A_b vary over frequency from 0 to 0.3. We chose this value of A_b so that the bifurcation term would be large enough to have a significant effect on the beam, but would not be wholly dominant over the main Gaussian component. The azimuthal offset angle, ϕ_1 , is set to either 0° or 90° so that we can observe the effects of both bifurcation orientations as the beam interacts with the sky.

Figure 3.5 shows the bifurcation profile at 40 MHz for a bifurcation amplitude (A_b) of 0.3. The bifurcation is strongest at 69° in elevation, and descends rapidly to zero on either side.

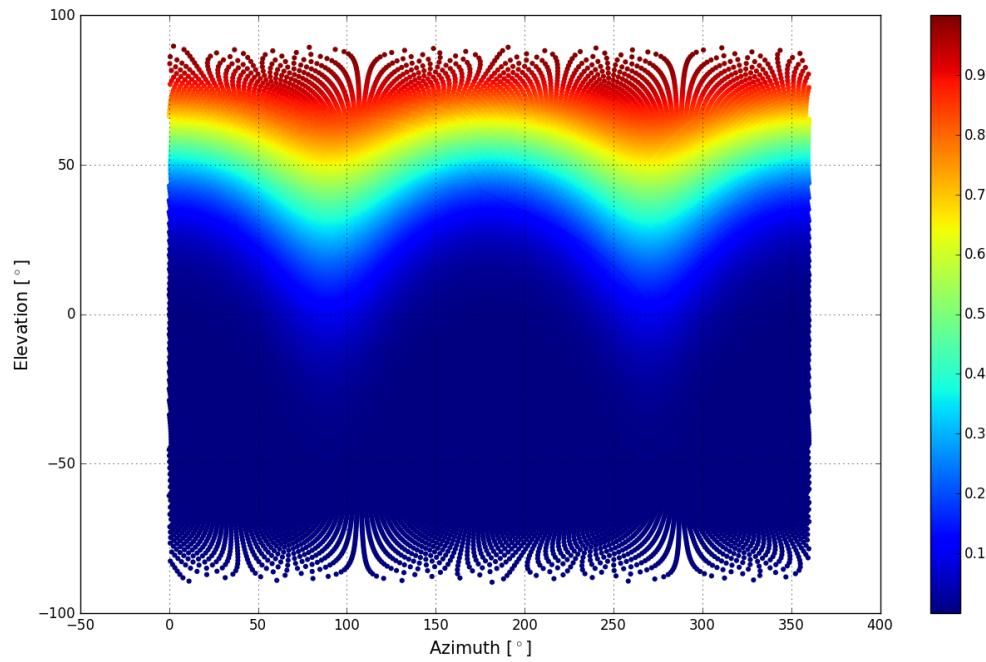


FIGURE 3.6: Normalized gain of an elliptical beam shown in antenna-centered local coordinates with an arbitrarily chosen rotation angle. The ellipticity of the beam causes nonuniform gain at a given elevation.

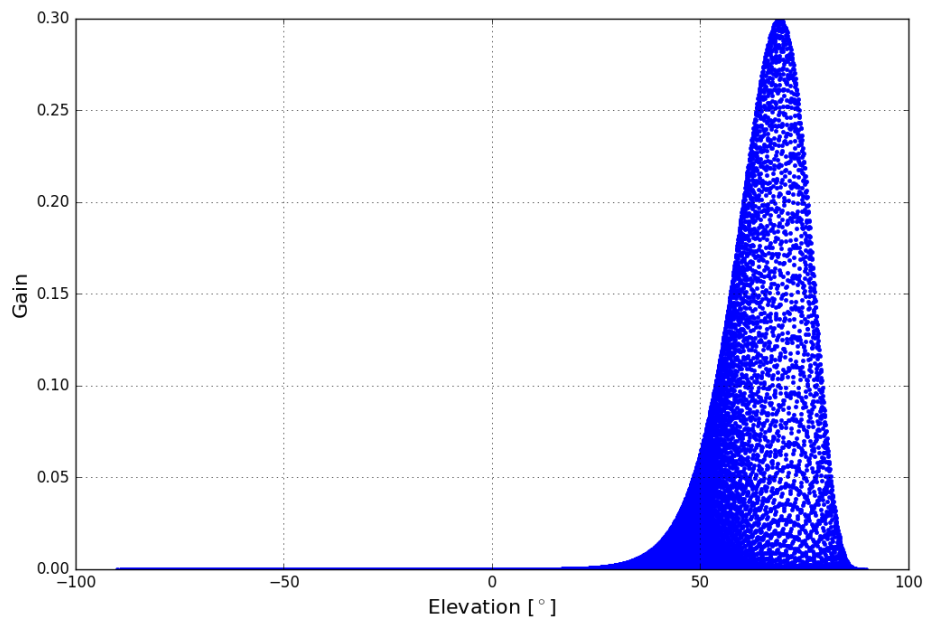


FIGURE 3.7: The bifurcation profile produced with Eqn. 3.6 and a bifurcation amplitude of 0.3. The gain is maximum at an elevation of 69° and descends rapidly to zero.

Figures 3.8 and 3.9 show an example of the normalized gain for a bifurcating beam with ϕ_1 set to 0° . The double peak of the gain is distinctly shown in Figure 3.8, and the dual nature of a bifurcating beam is reflected in the scatter plot of Figure 3.9.

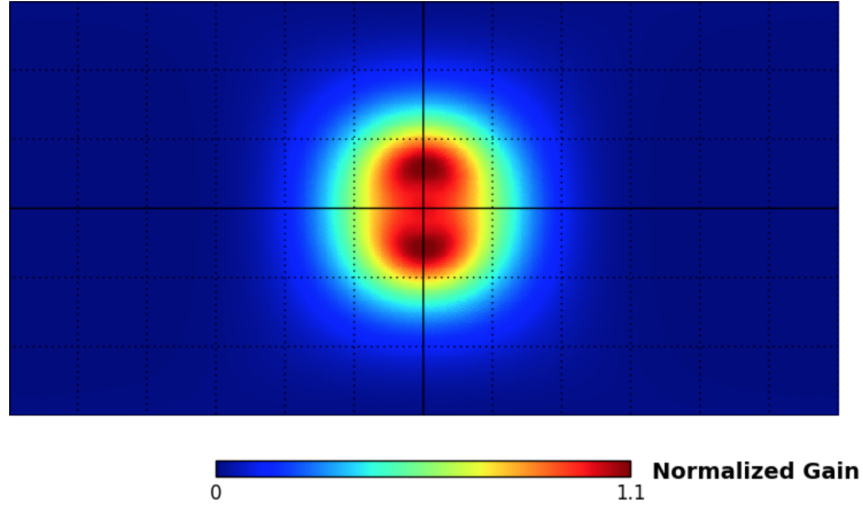


FIGURE 3.8: Gain of our bifurcated beam for a Gaussian amplitude of $A = 1$ and a bifurcating amplitude of $A_b = 0.3$, projected onto equatorial coordinates. The area enclosed by each grid again represents a 30° by 30° area.

To summarize this section, Table 3.2 shows the different frequency evolution options for the parameters in each beam type.

	A	σ_x	σ_y	A_b
Circular	✓	✓	✓	0
Elliptical	—	✓	✓	0
Bifurcated Gamma Distribution	—	—	—	✓

TABLE 3.2: Table showing different evolution options for each beam type, where ✓ represents the option for each variable to change linearly or as a quadratic and — signifies that the value is constant over the frequency band.

3.4 Details of Simulations

In this section we provide specific details about both the simulated beams and the low-foreground regions of the sky that we pointed to.

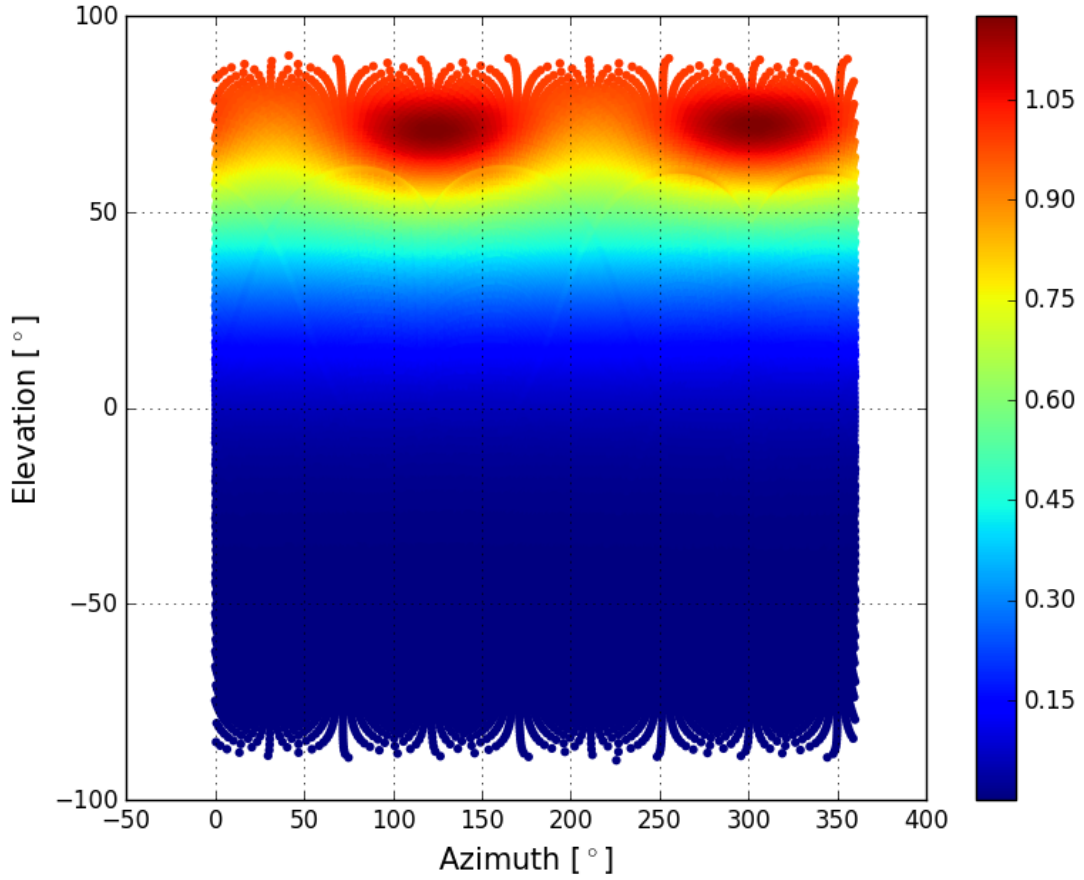


FIGURE 3.9: Normalized gain of our bifurcating beam for a Gaussian amplitude of $A = 1$, bifurcating amplitude of $A_b = 0.3$, and an arbitrarily chosen rotation angle, shown in antenna-centered local coordinates.

We picked three coordinate pairs to do our computations for the beam-sky convolution (Eqn. 3.1). We chose one low-foreground point to be in the Southern Hemisphere and one to be located in the Northern Hemisphere. As a reference, we also pointed at the Galactic Center, where we expect significantly higher sky temperatures. Table 3.3 provides the coordinates for the three points.

Point	Right Ascension [°]	Declination [°]
1	53	-26.7
2	165	33.9
Galactic Center	266	-29.33

TABLE 3.3: The three points for the beam simulations in equatorial coordinates.

We computed spectrally variant circular, elliptical, and bifurcating beams. Table 3.3 summarizes their parameter values.

Beam Types and Parameter Values					
Beam Type	A	$FWHM_x$ [°]	$FWHM_y$ [°]	Rotation Angle [°]	A_b
Circular	1 ± 0.1	90 ± 9	90 ± 9	—	0
Elliptical	1	63 ± 7	110 ± 11	0, 90	0
	1	70	110 ± 11	0, 90	0
Bifurcating	1	90	90	0, 90	0 - 0.3

TABLE 3.4: Parameter values used in the beam-sky convolution for all three beam types. The parameters evolve with frequency between the ranges shown.

Because, as modeled, the value of the Gaussian amplitude A is spatially independent, it can move outside the sums in the beam-sky convolution, and we therefore expect the spectral evolution of this parameter to cancel and have no effect on the convolution. Simulations of the convolution computed with varying A confirm this expectation, and we therefore neglect any further analysis of variations of this parameter for the remainder of this thesis.

The following tables show the beams we computed. Table 3.4 shows simulated circular beams, Table 3.5 shows the elliptical beams, and Table 3.7 shows the bifurcating beams.

Circular Beam		
Case	FWHM [°]	FWHM Evolution
0	90	Flat
1	90 ± 9	Linear, Positive Slope
2	90 ± 9	Linear, Negative Slope
3	90 ± 9	Quadratic, Positive Slope
4	90 ± 9	Quadratic, Negative Slope

TABLE 3.5: All cases of circular beam simulations. Case 0 is the nominal case, which we compare all other beams to.

A circular beam with a frequency-independent full width at half maximum (Case 0 in Table 3.4) was the nominal case in the simulations, and we compare the other results with this nominal case.

Elliptical Beam					
Case	$FWHM_x$ [°]	$FWHM_y$ [°]	FWHM Evolution	Ratio	ϕ_0
1	70 ± 7	110 ± 11	Linear, Positive Slope	Locked	0°
2	70 ± 7	110 ± 11	Linear, Negative Slope	Locked	0°
3	70 ± 7	110 ± 11	Quadratic, Positive Slope	Locked	0°
4	70 ± 7	110 ± 11	Quadratic, Negative Slope	Locked	0°
5	70 ± 7	110 ± 11	Linear, Positive Slope	Locked	90°
6	70 ± 7	110 ± 11	Linear, Negative Slope	Locked	90°
7	70 ± 7	110 ± 11	Quadratic, Positive Slope	Locked	90°
8	70 ± 7	110 ± 11	Quadratic, Negative Slope	Locked	90°
9	70	110 ± 11	Linear, Positive Slope	Changes	0°

TABLE 3.6: List of elliptical beams used in our simulations.

Although we computed all elliptical and bifurcating beams for both rotation angles (0° and 90°), for brevity, we consider only cases with a rotation angle of 0° . Likewise, though we experimented with beams that had changing ratios of F_x to F_y , we analyze only the cases with a locked ratio (Cases 1-4 in Table 3.6). We leave analysis of rotated beams and beams with unlocked ratios for future work.

Bifurcating Beam		
Case	A_b Evolution	ϕ_0
1	Linear, Positive Slope	0°
2	Linear, Negative Slope	0°
3	Quadratic, Positive Slope	0°
4	Quadratic, Negative Slope	0°
5	Linear, Positive Slope	90°
6	Linear, Negative Slope	90°
7	Quadratic, Positive Slope	90°
8	Quadratic, Negative Slope	90°

TABLE 3.7: List of bifurcating beams used in our simulations.

The results of these simulations convolved with our model sky are discussed in the following section.

3.5 Results and Discussion

We computed beam-sky convolutions (Eqn 3.1) for the beam cases listed in Section 3.4. This section analyzes and discusses the results of these simulated antenna temperatures.

3.5.1 Comparisons of Antenna Temperatures

We first analyzed the results of the antenna temperature for each case computed as compared to the antenna temperature of the nominal case (Case 0 in Table 3.4). We accomplish this by subtracting the nominal antenna temperature from the antenna temperature from beam i :

$$\Delta T_A = T_i - T_0 \quad (3.7)$$

We computed ΔT_A for Points 1 and 2, as well as at the Galactic Center. We started our analysis by comparing ΔT_A for for the three points in Table 3.3 using the nominal beam. We found that Points 1 and 2 have ΔT_A that are very similar (within 160 K of each other), and thus for clarity we focus primarily on the results of Point 1, which is the coordinate point located in the Southern Hemisphere. We chose this point because it is in a low-foreground region, and measurement attempts of the 21 cm signal point at regions with the smallest diffuse Galactic emission. Moreover, many experiments that are attempting to measure the 21 cm signal, such as EDGES and the Murchison Widefield Array, are located in the Southern Hemisphere on Earth, and thus the computations in this chapter will be more relevant for Point 1. As a reference, Figures 3.10 and 3.11 show ΔT_A between Point 1 and Point 2 and between Point 1 and the Galactic Center, respectively.

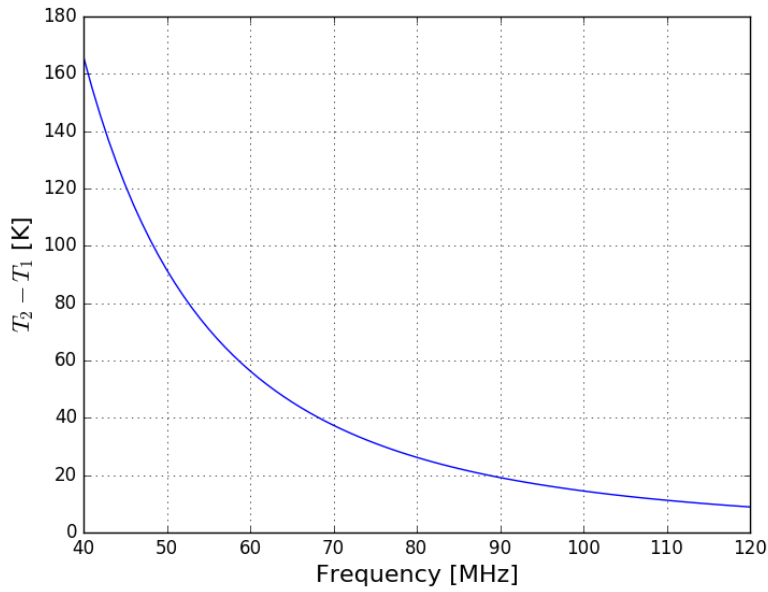


FIGURE 3.10: The difference between the antenna temperature at Point 2 and Point 1 for the nominal circular beam. ΔT_A is positive at all times because Point 2 has stronger foregrounds than Point 1, though the two points are comparable. The temperature difference is smooth over frequency.

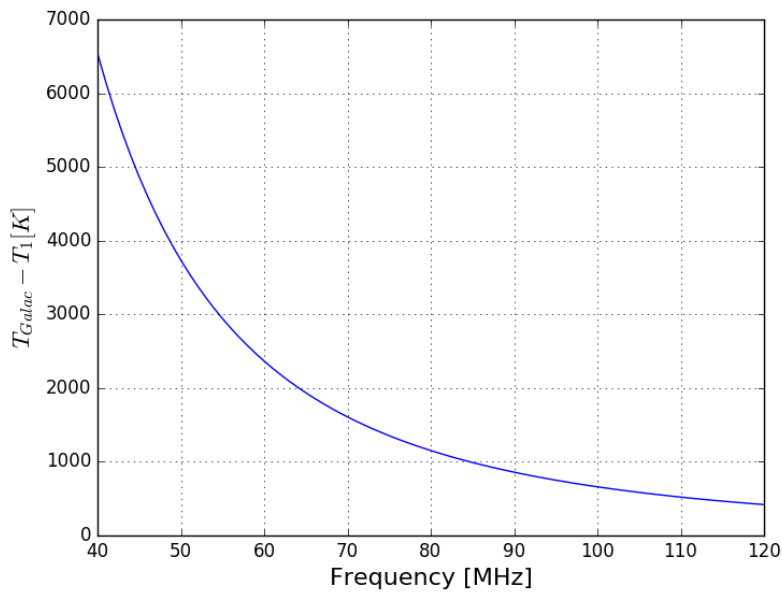


FIGURE 3.11: The antenna temperature difference between the galactic center and Point 1 for the nominal circular beam. As expected, the difference in temperature is thousands of Kelvin due to the high intensity at the Galactic Center. Again, the antenna temperature difference is smooth in frequency.

The following figures show the difference in antenna temperature between the nominal case and each beam type (circular, elliptical, and bifurcating). Figure 3.12 shows ΔT_A for the circular beams. We analyze this plot by looking at the cases with a positive slope (blue and red lines). At the low frequency end, these beams have a relatively small width, and they increase width with frequency, eventually growing larger than the nominal case. As the beam increases with frequency, the field of view increases, and thus ΔT_A increases in magnitude. Although ΔT_A increases monotonically, it saturates. This suggests that once the beam passes a certain value in width it continues its frequency evolution at the same rate as the nominal beam.

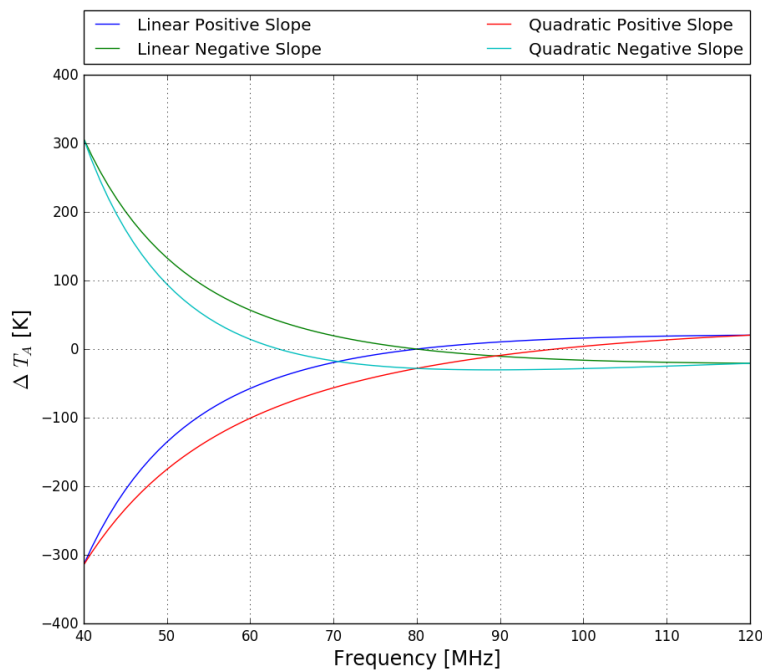


FIGURE 3.12: The differences in antenna temperature between the circular beams and the nominal beam. The differences are larger at low frequencies, presumably due to the higher sky temperature.

Figure 3.13 shows the differences in antenna temperature produced between elliptical beams (Cases 1-4 in Table 3.5). This type of simulated elliptical beam has a larger gain than the nominal case in one direction and a smaller gain in the other for the entire frequency range. By analyzing Figure 3.13, we can deduce that our elliptical beam with zero rotation (aligned parallel to the North-South axis) and a positively changing slope observes a sky with a much lower average temperature at low frequencies because its size and ellipticity allows it to avoid sky regions with

high temperature. The ellipticity of the beam blocks observations of high foreground regions of the sky, resulting in a large negative value of ΔT_A . Thus, in order to reduce the impact of foregrounds, for Point 1 it would be preferable to observe the sky with a beam that is elliptical along the North-South axis than with the nominal circular beam.

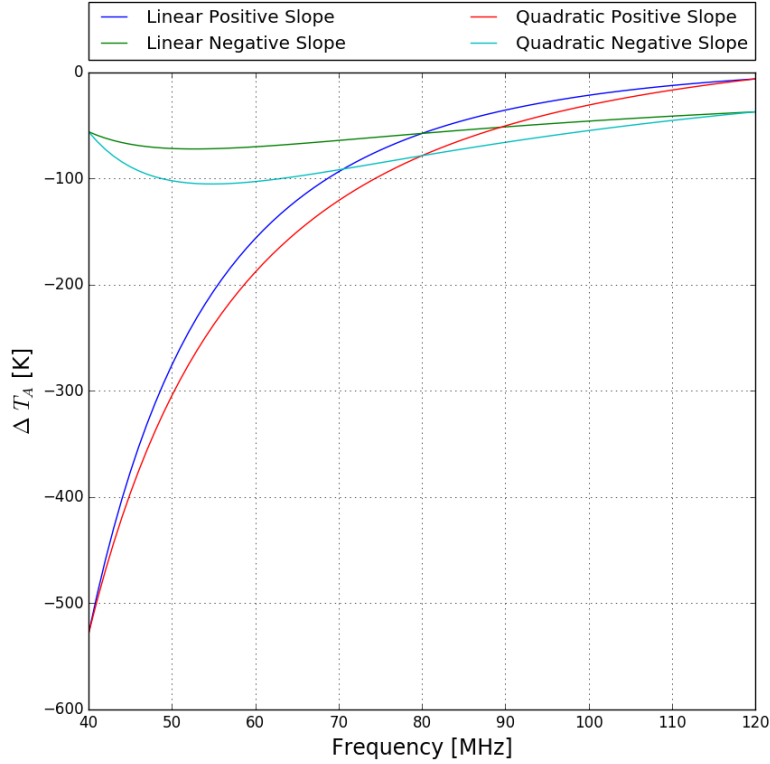


FIGURE 3.13: The differences in antenna temperature for an elliptical beam with a locked ratio, ϕ_0 equal to 0° , and F_y larger than F_x . At low frequencies and for a positive slope, ΔT_a is much lower than for the circular beams, meaning that this beam observes a region of the sky with lower average temperatures.

The differences in antenna temperature between the nominal case and a bifurcating beam are shown in Figure 3.14. Since ΔT_A is negative for all cases computed, we can infer that the gain structure of the bifurcating beam represents a weighting that produces a lower antenna temperature than the nominal case. Clearly, this difference is smaller than for the elliptical beams (Figure 3.9), which is to be expected. This is because in the nominal case and the bifurcating beam, the Gaussian full width at half maximum is nominally the same and frequency-independent. The small temperature difference is due to the evolving bifurcating component. For a bifurcating beam, the coordinates of the maximum gain are evolving in frequency, and because

ΔT_A is negative for all values in Figure 3.14, we can deduce that the maximum gain occurs at coordinates with lower sky temperature.

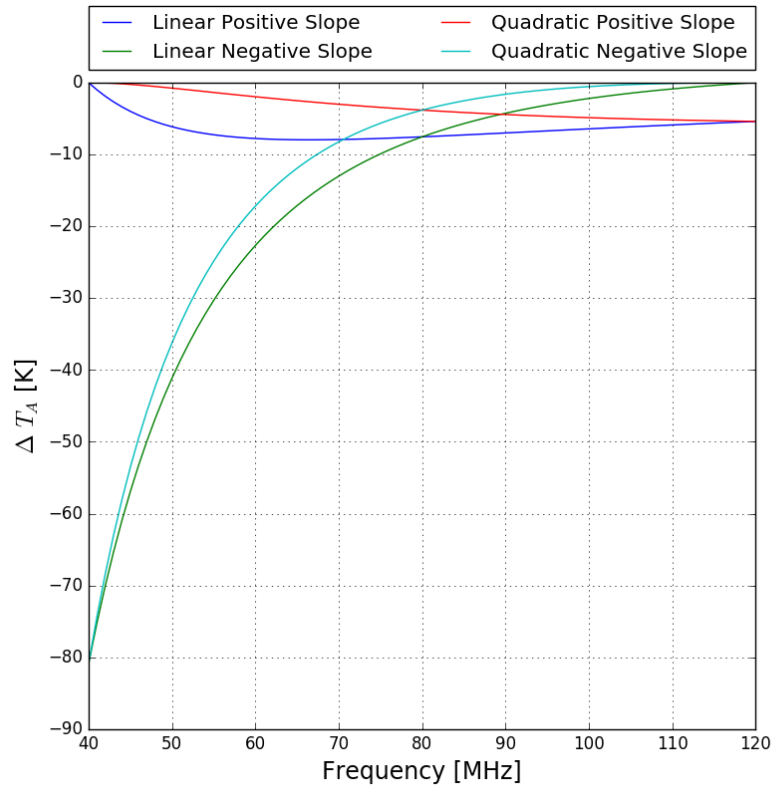


FIGURE 3.14: The differences in antenna temperature between the nominal beam and a bifurcating beam with a rotational offset of 0° aligned with the North-South axis.

3.5.2 Polynomial Fitting of the Antenna Temperature

In order to more quantitatively analyze the spectral content in each beam-sky convolution, we next use the Numpy functions Polyfit and Polyval to fit a polynomial to each simulated antenna temperature. We first fit a six term log-log polynomial for every case. We chose a log polynomial because it has been shown that it models realistic antenna temperature adequately [Harker et al., 2012]. If we chose a higher-order polynomial than one with six terms, the residuals would be too small for us to effectively differentiate between the effects of each beam type on the antenna temperature. Conversely, a polynomial with too few terms would not model properly the large spectral properties in the convolution (i.e, the intrinsic sky temperature),

making the comparison also very challenging. Our log polynomial has the following form:

$$\text{Log}(T_{sky}) = \sum_{i=0}^5 a_i \text{Log} \left(\frac{\nu}{\nu_n} \right)^i \quad (3.8)$$

We then computed the difference between each antenna temperature and the polynomial model of the antenna temperature:

$$\Delta T_A = T_A - T_{A, Poly} \quad (3.9)$$

This ΔT_A gives the residuals of the polynomial fit. Though we are not correcting for antenna chromaticity in this thesis, a sufficiently low residual (which we estimate here at around 5 mK for a 6-term polynomial) represents an antenna that would not impede detection of the global 21 cm signal without such corrections. We also compute the Root Mean Square (*RMS*) of each ΔT_A as in Bernardi et al., 2015:

$$RMS = \sqrt{\langle \Delta T_A^2 \rangle} \quad (3.10)$$

where $\langle \dots \rangle$ denotes an average over frequency. The *RMS* allows us to quantify the residuals and make comparisons between computed antenna temperatures. A larger *RMS* signifies an antenna temperature that has sharper spectral structure [Mozdzen et al., 2016] and so cannot be as effectively modeled by a log-log polynomial.

Table 3.8 shows the *RMS* for the ΔT_A residuals computed for circular beams convolved with the sky for the three pointings shown in Table 3.2. Figure 3.12 shows the residuals plotted over frequency for each case shown in Table 3.8. The nominal case at each coordinate pair (Case 0 in Table 3.4) is shown in blue in each panel, and the beam-sky convolution for cases 1-4 are shown for Point 1, Point 2, and the Galactic Center.

Beam	Case	RMS [mK]
Point 1	0	1.24
	1	0.77
	2	0.74
	3	22.0
	4	15.11
Point 2	0	1.25
	1	1.50
	2	4.97
	3	50.98
	4	10.68
Galactic Center	0	1.04
	1	4.72
	2	12.19
	3	120.0
	4	39.59

TABLE 3.8: The root mean square (RMS) of ΔT_A for every case shown in Figure 3.12. We pointed each circular beam (see Table 3.5) at all three sky pointings (see Table 3.3).

By analyzing Figure 3.15, we can clearly see that Point 1 has the smallest residuals for both linear and quadratic frequency evolutions, while the Galactic Center has the largest ΔT_A . In this figure, the residuals are below 5 mK over the entire frequency band only for a beam at Point 1 with a linearly evolving *FWHM*. Although the other panels have ΔT_A 's that eventually converge to within 5 mK, they are too large at low frequencies and thus represent obstacles to the measurement of the cosmological signal. These observations can be seen quantitatively by referring to Table 3.8. The nominal *RMS* for each point is comparable, indicating that this beam case can be removed with the same accuracy, regardless of pointing. The *RMS* for beams that evolve quadratically (Cases 3 and 4) are significantly larger at all three points than beams that change linearly. In particular, Case 3 has an *RMS* that is markedly larger than all other beam cases at all three coordinate pairs. This signifies that beams that

evolve quadratically over the frequency range introduce spectral structure that cannot be easily removed by a polynomial fit, and thus would impede measurements of the global 21 cm signal.

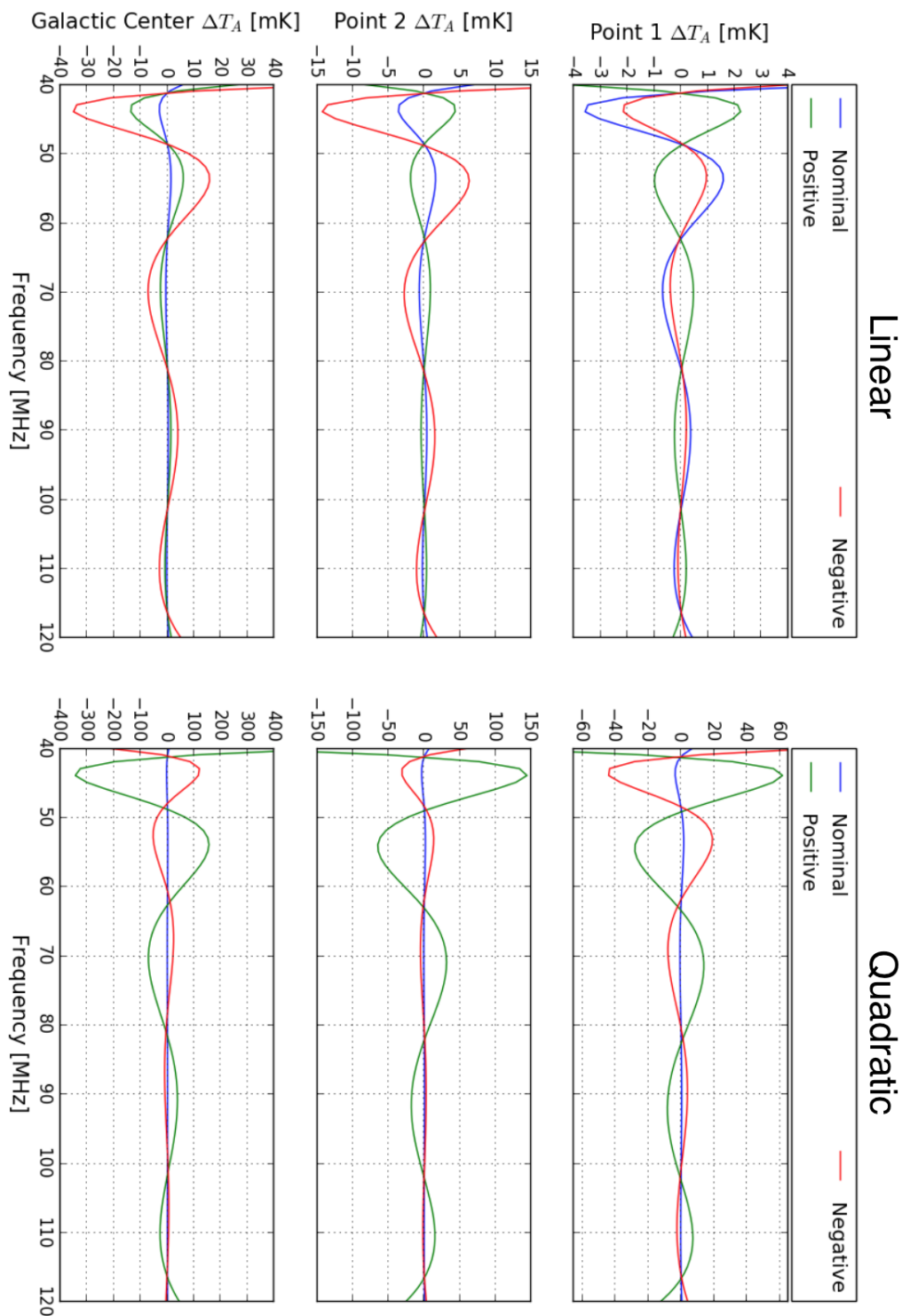


FIGURE 3.15: The residuals between the polynomial model of antenna temperature and the computed beam-sky convolution for the circular beams at all three sky pointings. The nominal beam as well as linear and quadratic spectral variations are shown for Point 1, Point 2, and the Galactic Center

Though Figure 3.15 is useful as a reference, for clarity, we again narrow our focus to the antenna temperature differences computed at Point 1. Figure 3.16 shows the residuals calculated at Point 1 for all three beam types with linear and quadratic spectral variations and a rotation angle of 0° (North-South orientation) for the bifurcating and elliptical beams. Each panel shows the nominal case (Case 0 in Table 3.4) at Point 1 in blue. The top two panels show the same linear and quadratic evolutions for a circular beam as Figure 3.15. Table 3.9 shows the corresponding *RMS* for each antenna temperature difference in Figure 3.16.

Beam	Case	<i>RMS</i> [mK]
Circular	0	1.24
	1	0.77
	2	0.74
	3	22.0
	4	15.11
Elliptical	1	0.16
	2	0.49
	3	10.81
	4	15.79
Bifurcating	1	1.35
	2	1.34
	3	2.08
	4	0.51

TABLE 3.9: The root mean square (*RMS*) of ΔT_A for every case shown in Figure 3.13, all of which are calculated at Point 1. See Tables 3.5-3.7 for details on each individual beam case.

For an elliptical beam (Cases 1-4 in Table 3.5), the residuals are sufficiently low for accurate measurement of the global signal in the linear case over the entire frequency band. However, for a quadratically evolving *FWHM* and constant ellipticity, they deviate to a maximum of 95 mK at 40 MHz. This is shown in Table 3.9, where the *RMS* for a quadratically beam evolving with a positive and negative slope is 10.81 and 15.79, respectively. In this case, though ΔT_A is constrained to within 5

mK at high frequencies, the beam variations would complicate the extraction of the cosmological signal over the entire frequency range. The *RMS* for each elliptical ΔT_A is substantially lower than that of a circular beam for every case except for a quadratic beam with a negative slope (Case 4), in which case the values are comparable. Therefore, because an elliptical beam has, on average, lower residuals than a circular beam, this beam type would be preferable to a circular beam when measuring the global 21 cm signal.

A bifurcating beam with linear evolution has residuals with an almost identical spectral shape as the nominal case. This indicates that these bifurcating beams do not introduce any structure that was not already present in the nominal beam case. Furthermore, a bifurcating beam with either a linear or quadratic evolution of A_b has residuals that are within the acceptable limit of 5 mK. In light of both these results and the antenna temperature shown in Figure 3.14, a bifurcating beam observing the sky at Point 1 should measure the 21 cm global signal most accurately out of all the cases analyzed. Since bifurcation is a common feature in real antenna beams, it is interesting to see that, by itself, bifurcation does not introduce substantial structure in the antenna temperature. Thus, within the assumptions made in this chapter, a bifurcating beam does not obstruct measurements of the global 21 cm signal.

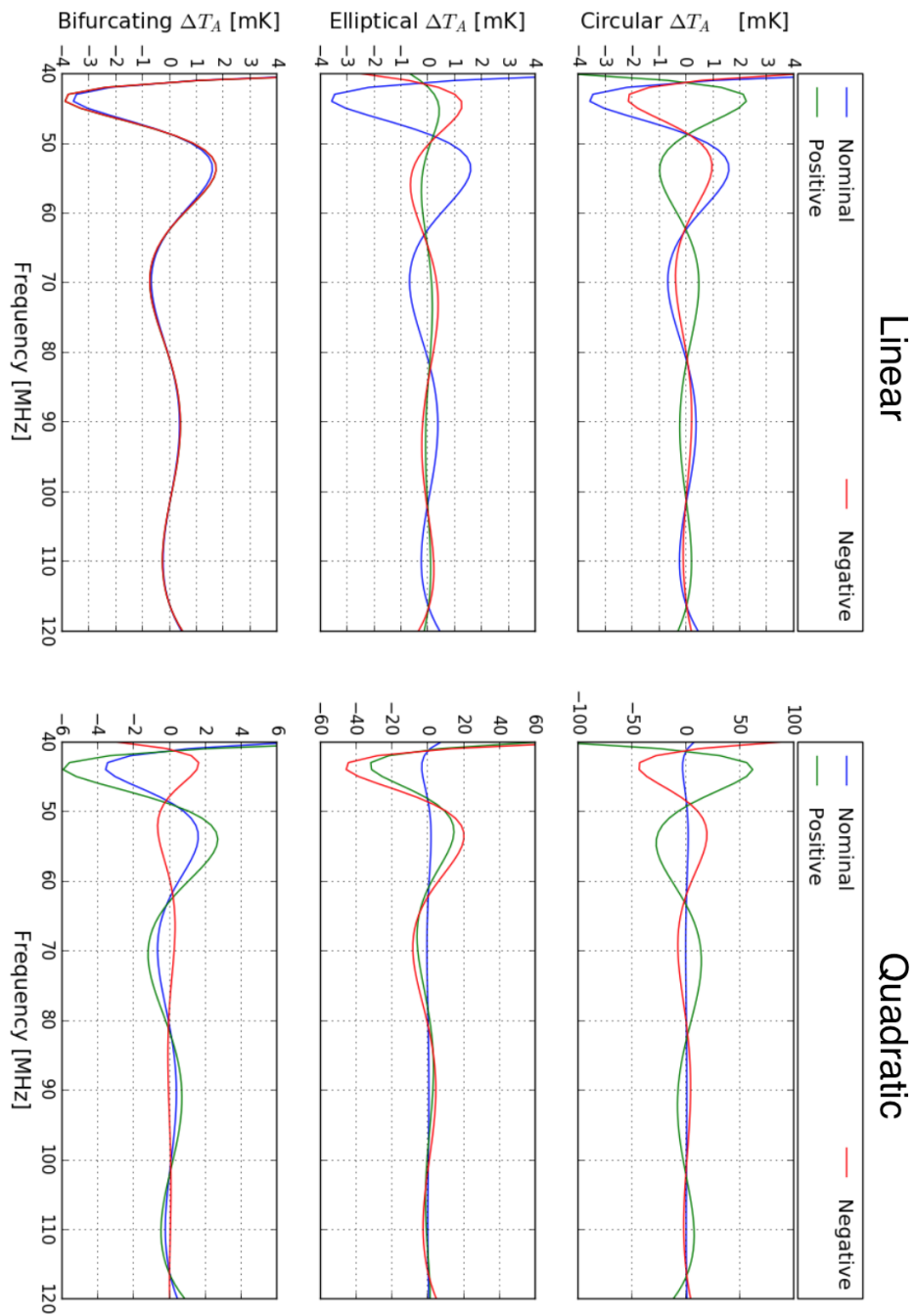


FIGURE 3.16: The residuals between the polynomial model of antenna temperature and the computed beam-sky convolution for all three beam types with both linear and quadratic spectral variations. Every case shown in this figure was computed at Point 1.

3.6 Summary

In Chapter 3 we explored the effect smoothly varying simulated beams had on the antenna temperature of the measurement instrument of the global 21 cm signal. We accomplished this by computing the beam-sky convolution of our simulated beams with a sky model to produce an antenna temperature that is accurate to first order. We simulated three beam types: circular, elliptical, and bifurcating, and analyzed how the antenna temperature of each beam compared to that of a nominal beam which was constant over the frequency range. We found that both elliptical and bifurcating beams had lower antenna temperatures than the nominal case, and thus deduced that these beams observed areas of the sky with lower temperatures. We also computed a six term log-log polynomial to fit the antenna temperature curve of each beam case. By subtracting this model of the antenna temperature from the actual computed temperature, we found the residuals for each beam type. Analysis of the residuals showed that, even without correcting for antenna beam chromaticity, beams that evolved linearly over the frequency range had residuals that were sufficiently low to avoid obstructing measurements of the global 21 cm signal. Elliptical beams that evolved linearly had both a lower antenna temperature and smaller residuals when fit with a polynomial than circular beams, and thus would introduce less structure into measurements of the cosmological signal. The rotation of an elliptical beam can also be chosen to block high temperature regions of the sky and thus produce a lower antenna temperature. Additionally, we found that the isolated effect of bifurcation does not introduce substantial structure into the antenna temperature, and therefore beams of this type would not impede measurements of the global 21 cm signal.

Chapter 4

Summary and Future Work

In this thesis we used analytical simulations to study two aspects of measurements of the global 21 cm signal. We first implemented a Fisher matrix analysis in Chapter 2 to estimate the uncertainties of cosmological parameters for simple measurement models with perfectly calibrated instruments. We find that, even when more parameters are incorporated in the measurement model to account for the Galactic foregrounds, the uncertainties of the cosmological parameters are constrained within 2% of the nominal values for measurement noise corresponding to 500 hours of observation time. Thus, under realistic models of noise and foreground emission, the parameters of our global 21 cm signal model can be effectively constrained with high precision. Simple models for this signal are still relevant because the 21 cm signal still has not been detected, and thus the cosmological parameter space remains completely unrestrained.

We also used a Fisher matrix method to explore the bias in the cosmological parameters due to measurement modeling errors. We computed the bias for simple frequency independent and frequency dependent model errors smaller than the global 21 cm signal, and found that the bias in our cosmological parameters was comparable to the statistical uncertainty due to measurement noise, thus making it insignificant. Though the model errors used in this thesis are not physically motivated, we used these computations as a way to verify that we were correctly implementing this Fisher matrix approach for bias calculations.

Future work using the Fisher matrix method to compute measurement uncertainties of the global 21 cm signal would incorporate increasingly more complex models of

the signal itself, the Galactic foregrounds, and the model errors in order to more accurately predict statistical and systematic uncertainties.

In Chapter 3 we simulated realistic antenna beams that varied smoothly over frequency and space to analyze the spectral structure they could introduce to measurements of the global 21 cm signal. We computed a weighted average of these beams with a synthetic sky model to find the antenna temperature spectrum, and we analyzed the results of this computation in two ways. First, we found the difference between the synthetic spectrum and a nominal spectrum that is generated using a frequency-independent beam, and we then quantified the spectral structure by fitting and removing a log-log polynomial to the antenna temperature. We found that, for the pointing coordinates used, beams that evolved linearly over the frequency range introduced the least amount of spectral structure. In addition, our simulations showed that linearly evolving elliptical beams had smaller residuals, and accordingly less spectral structure, than circular beams. We also found that a bifurcating beam had not only the smallest relative antenna temperature but also introduced the least amount of spectral structure, regardless of whether it evolved linearly or quadratically. Because of this, under the conditions simulated, a bifurcating beam would be the most ideal beam to use in measurements of the global 21 cm signal.

Future efforts would focus on effects of beam rotation on the antenna temperature. For the case of an elliptical beam, future work would involve exploring how a frequency dependent ellipticity affects computations of the beam-sky convolution.

Chapter 5

Bibliography

1. Bernardi, G., McQuinn, M., & Greenhill, L. J. (2015). FOREGROUND MODEL AND ANTENNA CALIBRATION ERRORS IN THE MEASUREMENT OF THE SKY-AVERAGED λ 21 cm SIGNAL AT $z \sim 20$. *The Astrophysical Journal*, 799(1), 90. <https://doi.org/10.1088/0004-637X/799/1/90>
2. Bernardi, G., Zwart, J. T. L., Price, D., Greenhill, L. J., Mesinger, A., Dowell, J., ... Schinzel, F. (2016). Bayesian constraints on the global 21-cm signal from the Cosmic Dawn. *Monthly Notices of the Royal Astronomical Society*, 461(3), 2847–2855. <https://doi.org/10.1093/mnras/stw1499> Celestial Equatorial Coordinate System - Basic Coordinates and Seasons - NAAP. (n.d.). Retrieved February 4, 2017, from http://astro.unl.edu/naap/motion1/cec_units.html
3. Coe, D. (n.d.). FISHER MATRICES AND CONFIDENCE ELLIPSES: A QUICK-START GUIDE AND SOFTWARE. Retrieved from <https://arxiv.org/abs/0906.4123>
4. Furlanetto, S. R., Peng Oh, S., & Briggs, F. H. (2006). Cosmology at low frequencies: The 21cm transition and the high-redshift Universe. *Physics Reports*, 433(4-6), 181–301. <https://doi.org/10.1016/j.physrep.2006.08.002>
5. Guzman, A. E., May, J., Alvarez, H., & Maeda, K. (2011). All-sky Galactic radiation at 45 MHz and spectral index between 45 and 408 MHz. *Astronomy & Astrophysics*, 525, A138. <https://doi.org/10.1051/0004-6361/200913628>
6. Harker, G. J. A., Pritchard, J. R., Burns, J. O., & Bowman, J. D. (2012). An MCMC approach to extracting the global 21-cm signal during the cosmic dawn from sky-averaged radio observations: Extracting the global 21-cm cosmic

- dawn signal. *Monthly Notices of the Royal Astronomical Society*, 419(2), 1070–1084.
<https://doi.org/10.1111/j.1365-2966.2011.19766.x>
7. Haslam, C. G. T., Salter, C. J., Stoffel, H., & Wilson, W. E. 1982, *A&A*, 47, 1
 8. LAMBDA - Foreground - Haslam 408 MHz All-Sky Map and Links. (n.d.). Retrieved February 4, 2017, from <https://lambda.gsfc.nasa.gov/product/foreground/haslam'408>.
 9. Monsalve, R. (2012, June 22). *Calibrations and Observations with the QUIET Radiotelescope* (Doctorate). University of Miami.
 10. Morales, M. F. (2005). Power Spectrum Sensitivity and the Design of Epoch of Reionization Observatories. *The Astrophysical Journal*, 619(2), 678–683.
<https://doi.org/10.1086/426730>
 11. Mozden, T. J., Bowman, J. D., Monsalve, R. A., & Rogers, A. E. E. (2016). Limits on foreground subtraction from chromatic beam effects in global redshifted 21 cm measurements. *Monthly Notices of the Royal Astronomical Society*, 455(4), 3890–3900. <https://doi.org/10.1093/mnras/stv2601>
 12. Mozden, T. J., Bowman, J. D., Monsalve, R. A., & Rogers, A. E. E. (2017). Improved measurement of the spectral index of the diffuse radio background between 90 and 190 MHz. *Monthly Notices of the Royal Astronomical Society*, 464(4), 4995–5002. <https://doi.org/10.1093/mnras/stw2696>
 13. Pritchard, J. R., & Loeb, A. (2011). 21 cm cosmology in the 21st century. *Reports on Progress in Physics*, 75(8), 086901. <https://doi.org/10.1088/0034-4885/75/8/086901>

Pritchard, J. R., & Loeb, A. (2010). Constraining the unexplored period between the dark ages and reionization with observations of the global 21 cm signal. *Physical Review D*, 82(2). <https://doi.org/10.1103/PhysRevD.82.023006>
 14. Thyagarajan, N., Parsons, A., DeBoer, D., Bowman, J., Ewall-Wice, A., Neben, A., & Patra, N. (2016). Effects of Antenna Beam Chromaticity on Redshifted 21 cm Power Spectrum and Implications for Hydrogen Epoch of Reionization Array. *The Astrophysical Journal*, 825(1), 9. <https://doi.org/10.3847/0004-637X/825/1/9>

15. van Haarlem, M. P., Wise, M. W., Gunst, A. W., Heald, G., McKean, J. P., Hessels, J. W. T., ... van Zwieten, J. (2013). LOFAR: The LOw-Frequency ARray. *Astronomy & Astrophysics*, 556, A2. <https://doi.org/10.1051/0004-6361/201220873>
16. Zaroubi, S. (2012). The Epoch of Reionization. In *The First Galaxies - Theoretical Predictions and Observational Clues*. Springer.